Enhanced electrochemical performance of supercapattery derived from sulphur-reduced graphene oxide/cobalt oxide composite and activated carbon from peanut shells

Delvina Japhet Tarimo, Kabir O. Oyedotun, Abdulmajid A. Mirghni, Bridget Mutuma, Ndeye Fatou Sylla, Phathutshedzo Murovhi and Ncholu Manyala*.

Department of Physics, Institute of Applied Materials, SARChI Chair in Carbon Technology and Materials, University of Pretoria, Pretoria 0028, South Africa.

*Corresponding author's email: ncholu.manyala@up.ac.za, Tel.: + (27)12 420 3549.

HIGHLIGHTS

•RGO-S and RGO-S/Co_3O_4 composites were successfully synthesized.

•Electrochemical performance of RGO-S has been improved by introduction of Co_3O_4.

•The RGO-S/Co_3O_4 was adopted as a positive electrode in a supercapattery device.

•The fabricated device demonstrate great potential for supercapacitors applications.

ABSTRACT

Sulphur-reduced graphene oxide/cobalt oxide composites (RGO-S/Co_3O_4) were successfully synthesized by varying mass loading of Co_3O_4 through a simple hydrothermal method. Structural, morphological, chemical compositional and surface area/pore-size distribution analysis of the materials were obtained by using XRD, Raman spectroscopy, SEM, TEM, EDX, FTIR, XPS and BET techniques, which reveal an effective synthesis of the RGO-S/Co_3O_4 composites. Electrochemical performance of the materials was evaluated using a three- and two-electrode system in 1 M KOH electrolyte. An optimized RGO-S/200 mg Co_3O_4 composite displayed the highest specific capacity of 171.8 mAh g^{-1} and superior cycling stability of 99.7 % for over 5000 cycles at 1 and 5 A g^{-1}, respectively, in a three-electrode system. A fabricated supercapattery device utilizing RGO-S/200 mg Co_3O_4 (positive electrode) and activated carbon from peanut shells (AC-PS) (negative electrode), revealed a high specific energy and power of

45.8 Wh kg^{-1} and 725 W kg^{-1}, respectively, at 1 A g^{-1}. The device retained 83.4 % of its initial capacitance for over 10, 000 cycles with a columbic efficiency of 99.5 %. Also, a capacitance retention of 71.6 % was preserved after being subjected to a voltage holding test of over 150 h at its maximum potential of 1.45 V.

KEY WORDS: Supercapattery, sulphur, graphene oxide, cobalt oxide composites, cycling stability, energy storage devices.

1. INTRODUCTION

The increase in population and advancement in technology has resulted in the high demand for power consumption. Currently, the well-known deficiency of fossil fuels and increasing environmental distresses are pushing researchers to adventure on sustainable, clean and readily accessible technology to supply and store energy [1,2]. This increases an interest to develop and design an efficient energy storage device. Batteries, supercapacitors and other energy conversions systems like hydrogen cells, fuel cells have been categorized as energy storage devices that can meet up the demand for technological advancements [3–5]. Supercapacitors have gained a considerable attention due to their high specific power, low cost, fast charge-discharge rate, and excellent cycling stability compared to batteries and conventional capacitors [6–8]. However, the practical application is limited by low specific energy compared to rechargeable batteries. This drives scientists to develop and design novel electrode materials which possess high electrochemical performance so as to increase supercapacitors' specific energy [9–11].

Owing to different charge storage mechanism, pseudocapacitors (PCs) and electrical double-layer capacitors (EDLCs) demonstrate a distinguished benefits for supercapacitors. PCs store charges through redox reaction which has high specific capacitance, but its application is

limited by poor charge transfer ability and shorter cycle life [12–14]. On the other hand, EDLCs store charges electrostatically on the surface of the electrode under constant potential, but, have low specific capacitance [1,15]. Therefore, by working with only one of them, it is difficult to manufacture a capacitor containing high energy and power densities. This challenge can be resolved by combining the advantages of both PCs and EDLCs through designing a hybrid electrode material with high capacitance and fast charge/discharge ability [9,16,17]. On the other hand, one can also form a hybrid device by combining a hybrid and an EDLC material working as a positive and negative electrode, respectively. The combination of these two materials with different charge-storage mechanisms and operating potentials could tailor the overall operating potential of the hybrid capacitor and hence improve its energy density [9,18–21]. Consequently, this type of energy storage device will be named as a hybrid or supercapattery device, depending on whether the final device shows mostly combination of pseudocapacitive and battery-type or pseudocapacitive behavior, respectively. The charge to voltage ratio remains the same throughout the cyclic voltammetry and charge/discharge curve for a capacitive material. However, for metals oxides and hydroxides such as Fe_2O_3, $Ni(OH)_2$, $MnCo_2O_4$, NiO, Co_3O_4 and $Co(OH)_2$, the ratio does not follow the former trend due the formation of redox peaks and thus are classified as battery-type materials instead of pseudocapacitive materials [5,22,23].

On the other hand, due to low specific energy, supercapacitors are still struggling to meet the demand for commercial applications. Thus, the awareness of combining features of supercapacitor and battery-type material in a single device where the end product is pseudocapacitive devise called supercapattery, paved the approach for improvement in electrochemical energy storage devices [24]. This combination produces a supercapattery device with high specific energy and power, and satisfactory cycle life than the traditional

carbon-based supercapacitors [25]. Therefore, supercapattery developed as an outstanding resolution intended for an electrochemical energy storage configuration which possesses the distinguishing features of advanced specific energy and power of batteries and supercapacitor, respectively. As a result, it decreases the specific energy gap between battery and supercapacitor [26,27]. Presently, most researchers are keen to improve the performance of supercapattery by merging together supercapacitors and batteries through designing a novel electrode materials with enhanced performance.

Mostly used electrode materials for supercapacitor applications include metal hydroxides, conducting polymers, metal oxides and carbon-based materials [13,28–30]. Recently, graphene and its derivatives namely, graphene oxide (GO) and reduced graphene oxide (RGO) have been used as electrode material for supercapacitor applications due to: 1) The properties of graphene can be enhanced by the addition of functional groups through utilizing the active sites contributed by the structural defects of graphene, 2) the electron transfer rate which can be promoted by electrical conductivity on the surface of graphene and 3) the agglomeration in graphene can be prevented by the flexibility of graphene nanosheets which offers sufficient space for the accommodation of different nanomaterials [4,31]. Despite these properties, the synthesis of graphene and its derivatives involve mostly chemical methods which consist of oxidation/reduction processes [32]. These methods affect the chemical structure of graphene due to the large number of radicals generated which in turn lower the electrochemical performance of the chemically modified graphene [21,33–36]. To overcome this drawback, heteroatom dopants such as sulphur can be incorporated into graphene matrix in order to increase the electrochemical performance of chemically modified graphene. Incorporation of S as a heteroatom by interstitials or substitutions create defects in graphene as a consequence of variations in graphene properties. It is known that C and S have small electronegativity

variation of 0.03 (carbon (2.55) and S (2.58)), thus increase in redox-active sites and chemical reactivity of graphene. Therefore, incorporation of S into graphene materials has been known to enhance wettability, improve surface properties and decrease charge transfer resistance [21,32,37–40].

Additionally, the electrochemical performance of reduced graphene oxide can be enhanced via the generation of metal oxide/S-reduced graphene composites. Typically, due to multiple oxidation states, transition metal oxides like iron (Fe), manganese (Mn), nickel (Ni), and cobalt (Co) oxides display excellent chemical and physical properties that enrich the electrochemical properties of supercapacitors [8,29,35,41]. Also, at higher oxidation states of transition metals, transition metal oxides produce more powerful alkaline corrosion protection compared to other materials [31,42]. Specifically, cobalt oxide (Co_3O_4) has been examined as a promising electrode material due to its high redox reactivity, easily tunable surface properties, simple preparation method, higher stability and cost effectiveness [8,34]. Co_3O_4 has Co^{3+} and Co^{2+} oxidation states positioned at octahedral and interstitial tetrahedral sites formed by oxygen ions in a closed packed face centered cubic structure, respectively. Thus offers high surface to volume ratios and faster charge transfer kinetics [23,43]. The p-type semiconductor and cubic spinel structure found in Co_3O_4 displays enhanced electro-active sites which makes it suitable for different applications such as electrochemical capacitors, sensors, Li-ion batteries and solar selective absorbers [12,42,44]. Moreover, Co_3O_4 has high redox behavior which contributes to high specific capacity/capacitance, but on the other hand, they are faced with low ionic/electrical conductivity. Also, during electrochemical reactions, they suffer from dissolution and aggregation resulting in a decrease in the number of active sites which hold back their capacitive behavior especially during repeated cycling and at high scan rate, hence rapid reduction of specific energy at high specific power [18,29,45,46].

The shortcomings can be resolved by combining Co_3O_4 and an improved graphene oxide which is anticipated to have high conductivity. This shortens the diffusion length for charge carriers and produces an electrode material with better electrochemical properties [29,33,47]. The bond formed by the interaction between graphene oxide and Co_3O_4 support in decreasing particle aggregation and ultimately improving the cyclic stability of the material. Furthermore, it can ease diffusion rate and ionic mobility, and hence improve the overall electrochemical properties. Therefore, electrochemical performance is expected to improve via the combined effects of the two materials in a composite formation by identifying the exact amount for each material in the composite [9]. Moreover, previous reports have indicated an improvement in the capacitive performance of the composites of metal oxides than individual oxide materials [48,49]. Additionally, most of the studies have reported on graphene/reduced graphene oxide with Co_3O_4 composite by mixing the whole precursor with other constituents (impurity) whereby it is difficult to figure out the exact amount of pure individuals to be mixed to form a composite [3,8,14,45,46,50].

In this study, a simple hydrothermal method with easily controllable parameters like concentration of the reagent, pH, temperature and time was applied to synthesize sulphur-reduced graphene oxide/cobalt oxide composites (RGO-S/Co_3O_4) by varying the mass loading of Co_3O_4. Each material was synthesized separately in order to ensure the purity of each sample and the exact amount of each component used to form a composite. This method proved to improve the charge storage capacity of the composite material. To the best of our knowledge, the use of sulphur-reduced graphene oxide/cobalt oxide (RGO-S/Co_3O_4) composite as electrode material for supercapattery device and produced by a high degree of synthetic control during synthesis has been rarely reported.

The successful synthesis of RGO-S/Co_3O_4 composite was confirmed by different characterization techniques. An optimized RGO-S/200 mg Co_3O_4 composite in a half-cell using 1 M KOH electrolyte displayed the highest specific capacity of 171.8 mAh g^{-1} and superior stability of 99.7 % for over 5000 cycles at 1 and 5 A g^{-1}, respectively. The fabricated supercapattery device demonstrated high specific energy of 45.8 Wh kg^{-1} with a corresponding specific power of 725 W kg^{-1} at 1 A g^{-1}. This supercapattery device also demonstrated excellent stability from both cyclic and voltage holding stability tests. The synergetic effect of the two materials was observed to improve the specific capacity, cyclic stability and rate capability which eventually increased the electrochemical performance of the supercapattery device.

2. EXPERIMENTAL

2.1 Synthesis of sulphur-reduced graphene oxide (RGO-S)

Sulphur-reduced graphene oxide was synthesized using modified Hummer's method as explained in our previous work [51]. Briefly, a polysulphide solution was formed by mixing 1 g of sulphur and 3 g of sodium sulphide (Na_2S) in 100 mL of deionized (DI) water and sonicated for homogeneity. Then, 2 mL of hydrochloric acid (HCl) was added into a solution formed by dissolving 50 mg of L-ascorbic acid in 12 g of DI water. Thereafter, 3 g of RGO, the polysulphide solution and L-ascorbic acid solution were combined and sonicated for 2 h for homogeneity. The mixture was stirred at 40 ^oC for 1 h and allowed to settle down for separation. The sample was washed several times with DI water, centrifuged three times at 10,000 rpm for 10 min and later freeze-dried for 24 h.

2.2 Synthesis of cobalt oxide (Co_3O_4)

Precipitation method was acquired to produce Co_3O_4 sample. 8 g of $CoNO_3$ was added into 400 mL of DI water and stirred for 15 min. Thereafter, 56 mL of 1 M NaOH was added

dropwise into the mixture which changed the color from pink to dark greenish color. $CoNO_3$ precursor was used as a source of cobalt while 1 M NaOH was used for polymerization and maintain the pH of 10 in the mixture while stirring for 2 h. The obtained mixture was decanted and washed several times with DI water, centrifuged at 10,000 rev/min for 10 min followed by drying in the oven at 60 ^oC for 12 h. The dried sample was later annealed in air for 2 h at 800 ^oC (5 ^oC/min) to remove the OH group and any possible impurities. Equation 1 and 2 below shows a complete reaction for obtaining Co_3O_4.

$$Co(NO_3)_{2(s)} + 2NaOH_{(l)} + H_2O_{(l)} \rightarrow Co(OH)_{2(s)} + 2NaNO_{3(aq)} + H_2O_{(l)} \quad (1)$$

$$3Co(OH)_{2(s)} \xrightarrow{annealed\ in\ air} Co_3O_{4(s)} + 2H_2O_{(g)} + H_{2(g)} \quad (2)$$

2.3 Synthesis of RGO-S/Co_3O_4 composite sample

The RGO-S/Co_3O_4 composite sample was prepared by adding 1 g of RGO-S and 100 mg of Co_3O_4 into 100 mL of DI water and sonicated for 1 h for homogeneity. Thereafter, the mixture was transferred into a Teflon-lined autoclave and heated in the oven at 150 ^oC for 1 h. The procedure was repeated by varying the mass of Co_3O_4 between 200 mg and 300 mg. The obtained mixture was allowed to settle down for easy separation. Later, it was washed several times with DI water and dried in the oven at 60 ^oC for 12 h.

2.4 Synthesis of activated carbon from peanut shell waste (AC-PS)

Activated carbon used in this study was produced from peanut shell waste as explained in our previous study [52]. In summary, two steps synthesis procedure was used to synthesize the material from peanut shell waste. Initially, the raw material from peanut shell waste was pyrolyzed using argon gas at 600 ^oC for 2 h. Then, the raw material (peanut shell waste) and

activating agent (potassium hydroxide - KOH) were mixed in a mass ratio of 1:4. Thereafter, the mixture was activated at 850 ^{o}C for 1h and the recovered sample was named as AC-PS.

2.5 Characterization

The micrographs of the pristine and composite material were obtained by using Zeiss Ultra Plus 55 field emission scanning electron microscope (FE-SEM; Akishima-shi, Japan) operated at 2.0 kV, equipped with an energy dispersive X-ray (EDX) and JEOL-2100F transmission electron microscope (HRTEM FEI Tecnai-F30; Akishima-shi, Japan) operated at 200 kV. The phase structure of the as-synthesized materials was studied by X-ray diffraction (D8 ADVANCED Bruker; Gerulhe, Germany) with a reflection angle 2θ values ranging between 7 - 90^{o} in a step size of 0.03 at 40 mA and 40 kV using Cu radiation source. A WITec Confocal Raman Microscope (WITec alpha 300 RAS+, Germany), Laser wavelength 532 nm, laser power 4 mW and spectral acquisition time 120-s was used for Raman analysis to determine the degree of defects in the material. Fourier transform-infrared spectroscopy (FT-IR) evaluation was obtained by a Varian FT-IR spectroscopy in a wavelength range 500 – 4000 cm^{-1}. An X-ray photoelectron spectroscopy (XPS) analyser (Versa Probe 5000 spectrometer initiated with a 100 μm monochromatic Al-Kα exciting source) was utilized to study the electronic states of the surface elements present within the composite sample. The Nitrogen adsorption and desorption isotherms were measured by NOVA Touch LX^{6} version equipped with a quanta-chrome Touch-Win software analyser. All samples were degassed at 80 ^{o}C for 10 hours under high vacuum environment. The specific surface area was evaluated using Brunauer-Emmett-Teller (BET) method from the absorption/adsorption isotherms in the relative pressure range (P/Po) of 0.01 - 0.2 and pore size distribution was calculated by using DFT method.

2.6 Electrochemical characterization

The EC-Lab V1.40 software in a BioLogic VMP300 potentiostat (Knoxville TN 37,930, USA), was used to evaluate the electrochemical measurements of the as-synthesize sample via three- and -two electrode systems. For three-electrode measurements, electrode was prepared by adding three drops of N-methyl-2-pyrrolidone (NMP) on a mixture containing 80 % of the working material, and 10 % each of carbon acetylene black (CB - conducting agent) and polyvinylidene fluoride (PVDF - binder) to make a slurry. The nickel foam 1 x 1 cm used as a current collector was coated with the slurry and then dried in the oven at 60 ^{o}C for 12 h. The mass of a single electrode was estimated as 2.4 mg cm^{-2}. The measurements were carried out by using Ag/AgCl as a reference electrode, material as a working electrode and glassy carbon as the counter electrode in 1 M KOH electrolyte. For three-electrode evaluation, the cyclic voltammetry (CV) and galvanostatic charge/discharge (GCD) measurements were done at various scan rates (5 to 100 mV s^{-1}) and specific currents (1 to 5 A g^{-1}), respectively within a working potential range 0.0 V - 0.5 V and 0 V to -0.9 V for positive and negative electrodes, respectively. The electrochemical impedance spectroscopy (EIS) was assessed in an open circuit potential at a frequency range 10 mHz - 100 kHz. The specific capacity (Q_s - mAh g^{-1}) and columbic efficiency (C_E - %) of a single positive electrode was evaluated using Equation 3 and 4 from the GCD profiles, respectively [53,54]:

$$Q_s = \frac{\Delta t \times I_d}{3.6} \quad (3)$$

$$C_E = \frac{t_D}{t_C} \times 100\,\% \quad (4)$$

where; I_d stands for applied specific currents (A g^{-1}), Δt represents the discharge time (s), t_D and t_C - discharge and charge time with the same current, respectively.

For two-electrode evaluation, the RGO-S/200 mg Co_3O_4 composite was used as a positive electrode and activated carbon from peanut shells (AC-PS) which shows ELDC behavior as a

negative electrode in 1 M KOH electrolyte. The mass on each electrode was estimated via the charge balance equation, as shown below [23,53,54]:

$$Q_+ = Q_- \Longrightarrow 3.6\, m_+ \times Q_{s+} = m_- \times \Delta V_- \times C_{s-} \Longrightarrow \frac{m_-}{m_+} = \frac{3.6\, Q_{s+}}{\Delta V_- \times C_{s-}} \quad (5)$$

where; Q_{s+} - specific capacity for the positive electrode, C_{s-} specific capacitance for the negative electrode, ΔV_- - potential window for the negative electrode, Q_+ and Q_- are charge for positive and negative electrode while m_+ and m_- stands for masses (mg) for the positive and negative electrodes, respectively.

The potential window of 1.45 V was reached by the fabricated supercapattery device. The following expressions were applied to evaluate the specific capacitance (C_s), specific energy (E_d) and specific power (P_d) of the device [20,50]:

$$C_s = \frac{\Delta t \times I_d}{\Delta V} \text{ [F g}^{-1}\text{]} \quad (6)$$

$$E_d = \frac{1}{2} C_s \Delta V^2 = \frac{C_s \times \Delta V^2 \times 1000}{2 \times 3600} = \frac{C_s \times \Delta V^2}{7.2} \text{ [Wh kg}^{-1}\text{]} \quad (7)$$

$$P_d = \frac{E_d}{\Delta t} \times 3600 \text{ [W kg}^{-1}\text{]} \quad (8)$$

where ΔV - operating potential (V), I_d - applied specific current (A g^{-1}), C_s - specific capacitance, Δt - discharge time (s), E_d - energy density and P_d - power density.

3. RESULTS AND DISCUSSION

Fig. 1 presents SEM and TEM micrographs acquired for the pristine and composite samples. Fig. 1 ((a, b), (d, e) and (g, h)) display the morphology of RGO-S, Co_3O_4 and RGO-S/200 mg Co_3O_4 composite (as an example of other composites which show similar morphology) in low and high magnification, respectively. The micrographs revealed that RGO-S comprises of nanorods/fibres and nanosheets like morphology (Fig. 1 (a, b)). Fig. 1 (d and e) displays a clear different morphology of Co_3O_4 with agglomerated nanograin-like structures, while RGO-S/200 mg Co_3O_4 (Fig. 1 (g and h)) show a combination of RGO-S and Co_3O_4 morphology. Fig. 1 (c,

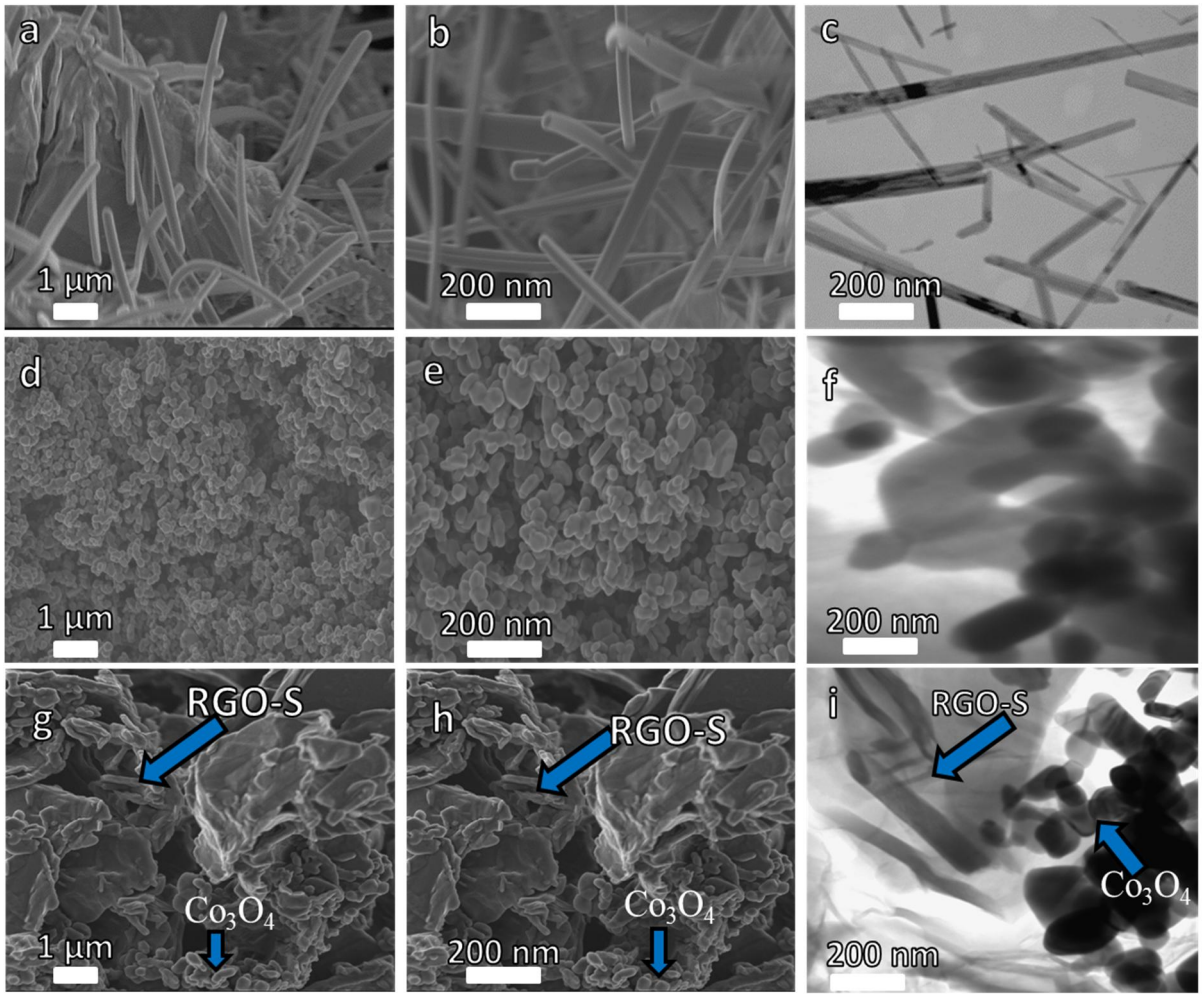

Fig. 1: (a, b), (d, e) and (g, h) are SEM images for RGO-S, Co_3O_4 and RGO-S/200 mg Co_3O_4 at low and high magnifications, respectively. (c, f and i) are TEM images for RGO-S, Co_3O_4 and RGO-S/200 mg Co_3O_4, respectively.

f and i) are TEM images of RGO-S, Co_3O_4 and RGO-S/200 mg Co_3O_4 composite, respectively at high magnification confirming the observations from SEM. It was also observed that the morphology of other RGO-S/Co_3O_4 composites remained the same regardless of the variation of mass loading 100 and 300 mg of Co_3O_4. However, with the introduction of Co_3O_4 into the active matrix of RGO-S, Co_3O_4 nanograins are seen to effectively attach themselves to the RGO-S nanorods/fibres and nanosheets, and formed a homogeneous and stable composite as shown in Fig. 1 (g and h). A uniform dispersion of the Co_3O_4 nanograins within the RGO-S nanorods/fibres and nanosheets is observed, which is vital for giving the essential surface required for effective electrochemical interactions. The uniform dispersion is contributed by

the use of hydrothermal method which allows for an even distribution of Co_3O_4 in the RGO-S matrix, and hence the observed morphology.

As an example (Fig. 2), further EDX measurements on RGO-S/200 mg Co_3O_4 were performed to show the elemental mapping and percentage of elemental composition within the material. Fig. 2 (a, b, c and d) displays the elemental mapping distribution of C, O, S and Co, respectively within the RGO-S/200 mg Co_3O_4 composite. Fig. 2 (e) displays the percentage by weight of each element in the composite sample, whereby, 62.10, 6.64, 25.67 and 5.59 Wt% was recorded for C, O, S and Co, respectively. Similar elemental distribution and composition were observed for RGO-S/100 mg Co_3O_4 and RGO-S/300 mg Co_3O_4 composites.

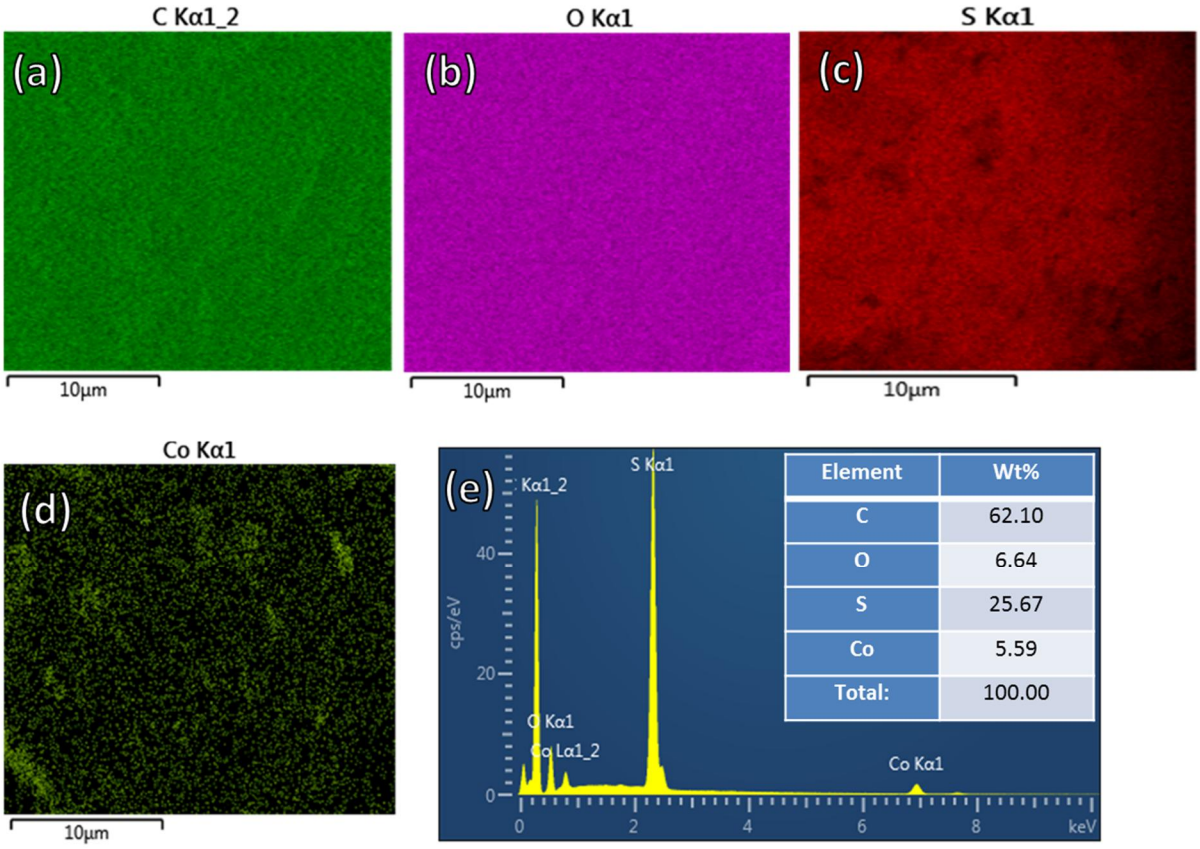

Fig. 2: (a, b, c and d) indicates the elemental mapping for RGO-S/200 mg Co_3O_4 composite as example and (e) it's corresponding EDS showing the percentage composition of the element within the material.

Rotational, vibrational and other low-frequency modes characterized by specific bonding in the materials were determined by Raman spectroscopy. Fig. 3 (a) displays the Raman spectra of the pristine sample (RGO-S) and all the composite samples (RGO-S/Co_3O_4 at various mass loading of Co_3O_4). The peaks observed at 1335 cm^{-1} and 1568 cm^{-1} correspond to D and G peaks of graphene, respectively, present in the pristine and the composites samples at different mass loading of Co_3O_4 [2]. The D peak indicates the existence of defects in the carbon matrix, while the G peak is a characteristic of sp^2 hybridized carbon in the graphene sheets. The I_d/I_g ratio signifies the level of defects in the material, which was estimated as 0.85 and 0.96 for RGO-S (pristine) and RGO-S/Co_3O_4 composites, respectively. This suggests a successful incorporation of Co_3O_4 within the RGO-S matrix and a good surface interaction of the two materials as confirmed by TEM morphology in Fig. 1 (i). The peak around 2674 cm^{-1} corresponds to 2D which developed from a second-order overtone due to a secondary inelastic scattering from a second phonon that distinguishes between monolayer and multilayer sheets of graphene within the material [3]. It was further observed that D, G and 2D band were able to maintain the same position for RGO-S and RGO-S/Co_3O_4 composites. However, the 2D intensity for the RGO-S/200 mg Co_3O_4 composite was noticed to have been reduced significantly as compared to the RGO-S and (100 and 300 mg) of Co_3O_4 composites revealing good interaction of Co_3O_4 nanograins with the RGO-S matrix because this band is very sensitive to the defects. It is also clear that D peak for this sample indicates more defective RGO-S where the intensity ratio of I_D to I_G is almost one as compared to the other samples. This is also the indication of a clear effect of good interaction of Co_3O_4 and RGO-S. The peaks around 486 and 653 cm^{-1} indicates E_g and $A1_g$ vibration modes of Co_3O_4, respectively [55]. These modes indicate coordination between Co and O atoms whereby cations and anions allocation on the spinel of Co_3O_4 is displayed as Co^{2+} [Co_2^{3+}] O_4^{2-}. The cations in the brackets are octahedral and those outsides are coordinated with oxygen anions tetrahedrally [56]. These

results show that Co_3O_4 was successfully incorporated into RGO-S matrix to form a composite material.

Fig. 3 (b) shows the phase structure analyzed by XRD displaying narrow and sharp peaks for the as-synthesized Co_3O_4, RGO-S, and RGO-S/Co_3O_4 composite with different mass loading of Co_3O_4 demonstrating high crystallinity of the material. The XRD spectrum at the bottom (black) is a clear indication of pure Co_3O_4 with the diffraction peaks around $2\theta = 18.9^o$, 31.2^o, 36.7^o, 44.9^o, 59.3^o and 65.1^o which corresponds to (111), (220), (311), (400), (511) and (440) planes, respectively. The XRD pattern of Co_3O_4 and its equivalent planes match well with the Joint Committee on Powder Diffraction Standards (JCPDS) card no. 42-1467 [12]. The observed diffraction peaks (red) around $2\theta = 11.4^o$, 15.4^o, 22.9^o, 26.7^o, 27.7^o, 31.8^o, 36.9^o and 42.9^o corresponding to (001), (113), (222), (002), (313), (044), (422) and (100) planes, respectively, suggest the existence of RGO-S in the material. The XRD spectra of RGO-S match well with the JCPDS card nos. 89-4307 and N34-0941 for RGO and S crystal structures, respectively [51,57]. The XRD patterns for RGO-S/100 mg Co_3O_4 (blue), RGO-S/200 mg Co_3O_4 (dark cyan) and RGO-S/300 mg Co_3O_4 (magenta) composites shows some sharp peaks arising from RGO-S and Co_3O_4 revealing the successful growth of Co_3O_4 on RGO-S as observed in SEM images in Fig. 1 (g and h). Furthermore, the analysis confirmed that the crystal structure of the RGO-S was maintained during the composites formation (RGO-S/Co_3O_4).

FTIR spectroscopy is a tool that provides a report concerning the phase composition of the material, behavior regarding functional groups and how oxygen is attached to the metal ions. Fig. 3 (c) shows the FTIR spectra of the various samples as indicated in the figure, revealing surface functional groups of Co_3O_4, RGO-S, and RGO-S/Co_3O_4 composite materials. The -OH

stretching vibration is ascribed to the absorption peak spotted at 3428 cm^{-1} presenting the hydroxyl group. The peak at 1396 cm^{-1} is linked to tertiary C-OH group while 1656 cm^{-1} is attributed to the O-H bending vibrations of absorbed water molecules. Stretching vibration of epoxy group (C-O) is observed at 998 cm^{-1} while the sp^2 vibration of the graphene sheets is confirmed by the peak marked at 1572 cm^{-1} (C=C). The Co_3O_4 spinel structure of the Co-O bond for ABO (A-Co^{2+} tetrahedral site) and OB_3 (B-Co^{3+} octahedral site) vibrations matches with the FTIR peaks around 542 and 652 cm^{-1}, respectively [28,48,58].

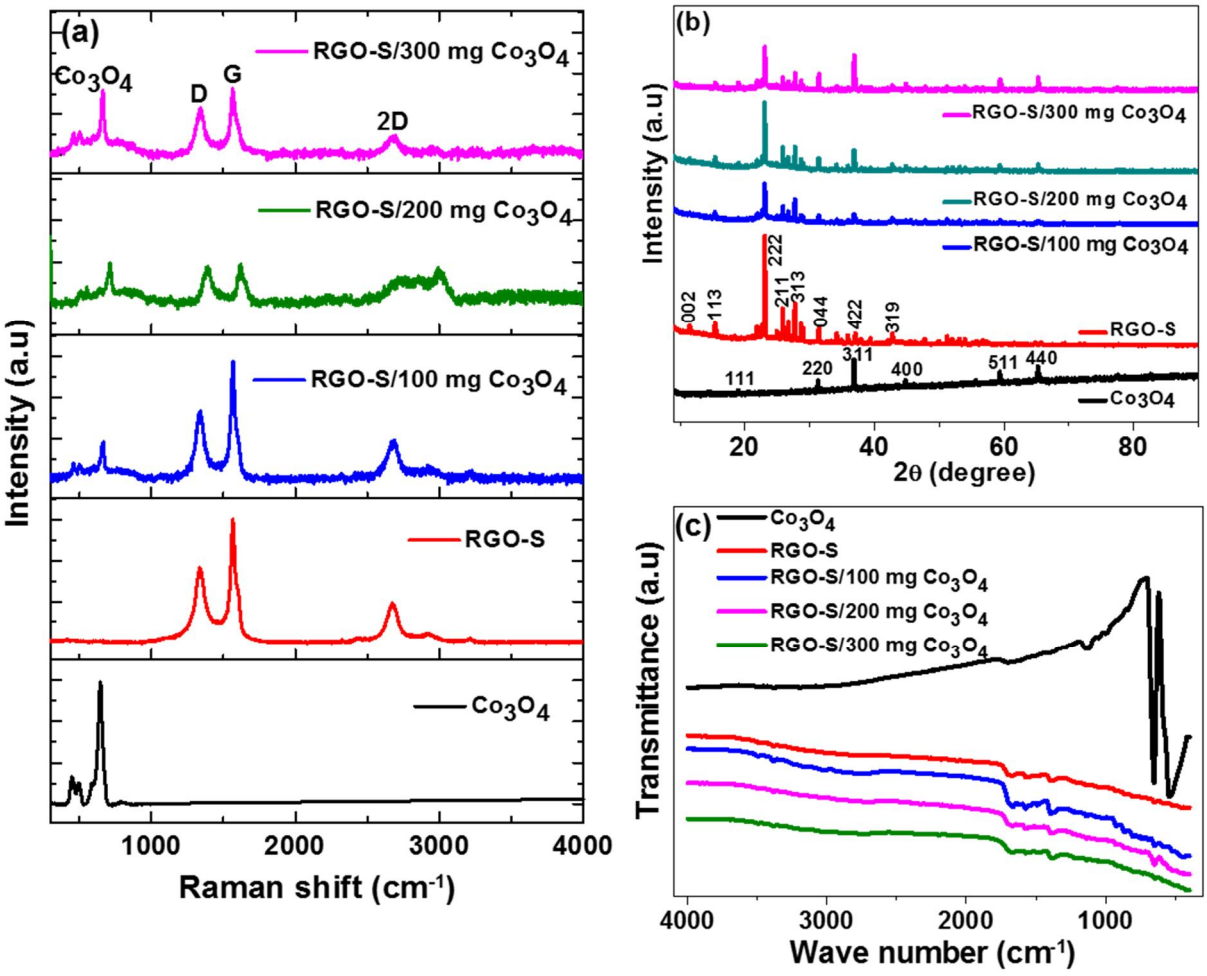

Fig. 3: (a) Raman, (b) XRD and (c) FTIR spectrum for Co_3O_4, RGO-S, RGO-S/100 mg Co_3O_4, RGO-S/200 mg Co_3O_4 and RGO-S/300 mg Co_3O_4, respectively.

The XPS analysis was used to acquire the information about the chemical states of the as-synthesized RGO-S/200 mg Co_3O_4 composite sample. Generally, the spectrum (intensity versus binding energy) is being generated by a photoelectrons emitted from the surface of the

tested sample by a monochromatic energies of Kα X-rays. The emitted lines are useful in determining the chemical states of the material through correlating the binding energy position and the intensity of each line in the material being analysed [26]. Fig. 4 (a) shows a wide scan of RGO-S/200 mg Co_3O_4 composite presenting a comprehensive surface elemental composition with major peaks of C 1s, O 1s, S 2p and Co 2p indicating the presence of carbon, oxygen, sulphur and cobalt elements in the material. The single peak of C 1s (Fig. 4 (b)) was further deconvoluted into four sub-regions with their binding energies at 284.2, 284.9, 285.8 and 287.9 eV corresponding to C=C (sp^2), C-C (sp^3), C-O and C=O bonds, respectively. The former two peaks shows the existence of non-oxygenated carbon atoms corresponding to sp^2 and sp^3 hybridized carbon while the later presents the hydroxyl and carboxyl functional groups present within the material [59]. The deconvoluted O 1s in Fig. 4 (b) presents three peaks at 529.6, 531.2 and 533.0 eV, corresponding to metal oxides, C-O and C=O bonds, respectively. The first peak (529.6 eV) is related to the lattice oxygen in a Co_3O_4 spinel structure while the rest of the two peaks are linked to the oxygen bonded to carbon, oxygen in cobalt hydroxides ions, cobalt monoxide and water adsorbed on the surface of Co_3O_4 [10]. The high resolution S 2p spectra in Fig. 4 (c) shows the formation of C-S-C single bond and C=S double bond at a binding energies of 163.3 eV and 164.4 eV, respectively [4,32,60]. This shows that sulphur atom was successfully incorporated into the composite sample. Fig. 5 (e) displays two forms of cobalt oxide (CoO and Co_3O_4), which can be recognised by the shakeup satellites at 779.9 and 795 eV which corresponds to Co $2p_{3/2}$ and Co $2p_{1/2}$, respectively. The gap between Co $2p_{3/2}$ and Co $2p_{1/2}$ is ~15.1 eV indicating the presence of standard Co_3O_4 spectra [59]. Additionally, there was existence of weak shake-up satellite peaks at 804.7 and 786.8 eV at higher binding energy. These specify that the composite is composed of Co_3O_4 and the oxygen connects between Co_3O_4 and RGO-S in the RGO-S/200 mg Co_3O_4 composite sample.

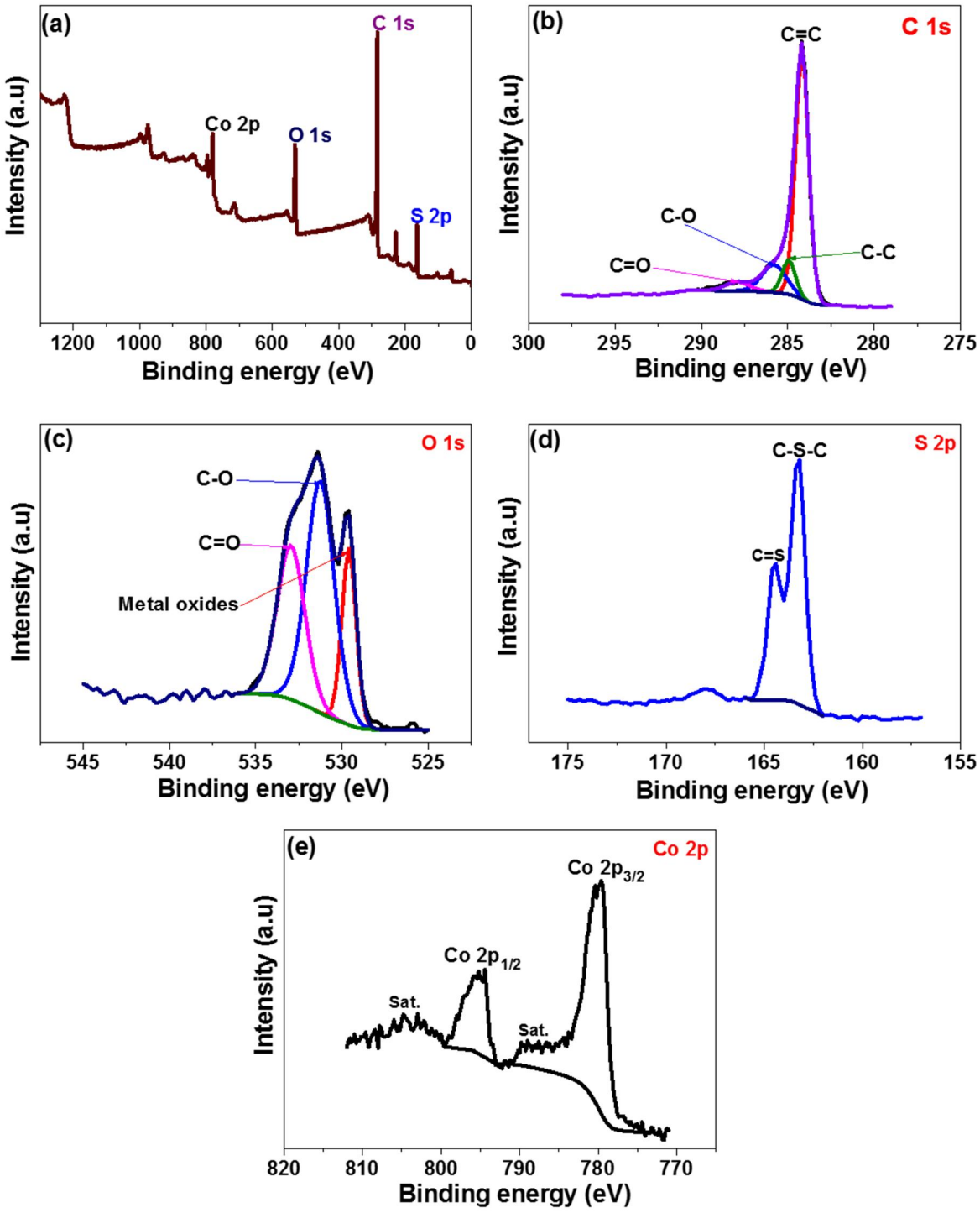

Fig. 4: (a) XPS survey spectra, core level spectrum of (b) C 1s, (c) O 1s (d) S 2p and (e) Co 2p of RGO-S/200 mg Co_3O_4 composite, respectively.

The nitrogen (N_2) gas adsorption/desorption investigation were conducted to evaluate the specific surface area and pore size distribution of the samples. Fig. 5 (a) and (b) displays the N_2 adsorption/desorption isotherms and pore size distribution calculated using DFT,

respectively, of RGO-S, RGO-S/100 mg Co_3O_4, RGO-S/200 mg Co_3O_4 and RGO-S/300 mg Co_3O_4, respectively. From Fig. 5 (a), shows the N_2 adsorption/desorption isotherms whereby the specific surface areas recorded for RGO-S, RGO-S/100 mg Co_3O_4, RGO-S/200 mg Co_3O_4 and RGO-S/300 mg Co_3O_4 composite were found to be 11.66, 10.38, 14.68 and 9.71 m^2/g, respectively. It can be observed that RGO-S/200 mg Co_3O_4 composite displays a higher specific surface area (14.68 m^2/g) compared to the other samples. This is the clear indication that this the right composition that both materials synergize optimum composition which facilitated the interaction between the two materials [5]. Therefore, it is expected to enhance the electrochemical performance of RGO-S/200 mg Co_3O_4 composite. As displayed in Fig. 5 (b), all the samples present a type-III behavior with an H3-type hysteresis loop signifying the existence of non-rigid aggregates of plate-like particles as it shown in the SEM images. Fig. 5 (b) shows the DFT pore size distribution. It is also clear here that RGO-S/200 mg Co_3O_4 shows more pore volume as compare to the rest of the other samples and hence still showing better performance.

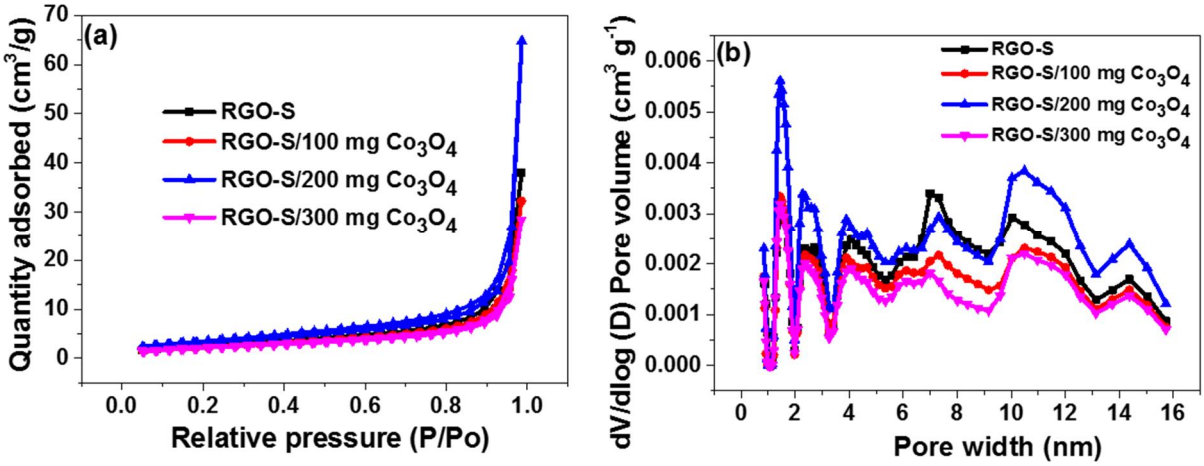

Fig. 5: (a) N_2 adsorption/desorption isotherms and (b) DFT pore size distributions of RGO-S, RGO-S/100 mg Co_3O_4, RGO-S/200 mg Co_3O_4 and RGO-S/300 mg Co_3O_4, respectively.

The cyclic voltammetry (CV) curves at 50 mV s^{-1} for RGO-S and RGO-S/Co_3O_4 composites at different mass loading of Co_3O_4 in a positive potential window range of 0.0 - 0.5 V vs Ag/AgCl is presented in Fig. 6 (a). The CV curves display a faradic behaviour confirming the redox reaction within the material. It was further noted that the RGO-S/200 mg Co_3O_4 composite shows higher current response compared to the RGO-S (pristine), RGO-S/100 mg Co_3O_4 and RGO-S/300 mg Co_3O_4. The higher current response displayed by RGO-S/200 mg Co_3O_4 confirms the material's high specific capacity as a result of good synergy between 200 mg of Co_3O_4 and RGO-S. The galvanostatic charge-discharge (GCD) in Fig. 6 (b), was further used to analyse the electrochemical performance of the RGO-S (pristine) and RGO-S/Co_3O_4 composites at 1 A g^{-1} within a positive potential range of 0.0 - 0.5 V vs Ag/AgCl. The non-linear GCD curves with a potential plateau indicates a clear correspondence between features displayed by GCD curves in Fig. 6 (b) to that of CV curves in Fig. 6 (a). The specific capacity evaluated through the GCD curves using Equation 3 at 1 A g^{-1}, was found to be 145.1, 79.7, 171.8, and 77.3 mAh g^{-1} for RGO-S, RGO-S/100 mg Co_3O_4, RGO-S/200 mg Co_3O_4 and RGO-S/300 mg Co_3O_4, respectively. Furthermore, the high specific capacity of RGO-S/200 mg Co_3O_4 was confirmed by the longest discharge time compared to other samples, as shown by the GCD curve in Fig. 6 (b), which corresponds with the high current response observed in the CV curve in Fig. 6 (a). This particular composition is the right amount of Co_3O_4 to have a positive impact on the RGO-S as compared with other mass loadings, which makes 200 mg mass loading the optimum amount.

Moreover, the charge-transfer resistance of the redox reactions, diffusive resistance of the electrolyte in the electrode, and ionic resistance of the electrolyte, was used to assess the capacitive performance of the as-synthesized materials by performing the EIS measurements. Fig. 6 (c) shows the EIS Nyquist plot of RGO-S and RGO-S/Co_3O_4 composites measured at a frequency range 10 mHz – 100 kHz. From the EIS; the composites with 100 and 300 mg show

long diffusion length with large deviation from the vertical line indicating more resistive behaviour and slow charge transport whereas the composite with 200 mg displays shorter diffusion length suggesting fast charge transport. The equivalent series resistance (ESR) value was experimentally determined from the x-axis intercept at high-frequency region as displayed in an inset to Fig. 6 (c). In the Nyquist plot, the intersection with the real Z′ axis is attributed to the equivalent series resistance (ESR) which is the total resistance of the ionic resistance of electrolyte, the electrolyte/electrode interface resistance and electrode/current collector interface resistance [40, 54]. The ESR provides information about the contact resistance between the working electrode and the current collector, and the interface resistance of the working electrode and ions from the electrolyte [40,54]. An ESR value of ~ 1.54 **Ω**, 1.62 **Ω**, 1.43 **Ω**, and 1.81 **Ω** were recorded for RGO-S, RGO-S/100 mg Co_3O_4, RGO-S/200 mg Co_3O_4 and RGO-S/300 mg Co_3O_4, respectively. It was further observed that RGO-S/200 mg Co_3O_4 has the smallest ESR value compared to the RGO-S (pristine sample), RGO-S/100 mg Co_3O_4 and RGO-S/300 mg Co_3O_4. All these signify the good synergy between RGO-S and this particular mass loading of Co_3O_4 which performs the function of improving the electrochemical performance of the as-synthesized composite.

The charge-discharge cycles over 5000 cycles, were performed as shown in Fig. 6 (d) indicating an excellent columbic efficiency (C_E - %) versus cycle number for RGO-S and RGO-S/Co_3O_4 composites samples at 5 A g^{-1}, respectively. The C_E (%) calculated using Equation 4 was found to be 99.2 %, 98.8 %, 99.7 % and 98.5 % for RGO-S, RGO-S/100 mg Co_3O_4, RGO-S/200 mg Co_3O_4 and RGO-S/300 mg Co_3O_4, respectively. From these results, a superior cycling stability of approximately 100 % was demonstrated by RGO-S/200 mg Co_3O_4 compared to other samples. This performance is contributed by the combination of RGO-S and 200 mg Co_3O_4 which has been seen to enhance the accessibility and transport of OH^- ions

during rapid charge-discharge process than an individual material. As a result, 200 mg Co_3O_4 was observed to act as a buffer for the volume change during charge-discharge and hence an improved stability in the RGO-S/200 mg Co_3O_4 composite [14,16,55,61].

In general, the RGO-S/200 mg Co_3O_4 composite was found to have high current response in the CV curve, longest discharge time in the GCD curve which shows high specific capacity, low ESR value and short diffusion length in the EIS Nyquist impedance, and high cycling performance compared to pristine and other composites samples, respectively. These observed excellent performances might be associated with the synergy between RGO-S and 200 mg Co_3O_4 mass loading in particular as supported by SEM, Raman and BET measurements. The SEM showed well uniformly distributed nano-grains of Co_3O_4 in the matrix of RGO-S nanorods/fibers (see Fig. 1 (g, h, i)). Raman spectra showed that 2D, which is very sensitive to defects is the most affected for this composite as compared to other samples, hence it's a clear indication of good interaction between the two materials (see Fig. 3 (a)). The BET measurements shows that this composite has much higher specific surface area and pore volume as compared to other samples (see Fig. 5). Therefore, these results shows that by controlling the amount of Co_3O_4 during the synthesis process has resulted into a composite with improved electrochemical performance. Hence, this study suggests that the easiest way of improving the performance of supercapattery electrode material is by focussing on the synthesis condition like the optimization of metal oxide mass loading ratio. From the above observations, RGO-S/200 mg Co_3O_4 was chosen as a positive electrode for device fabrication.

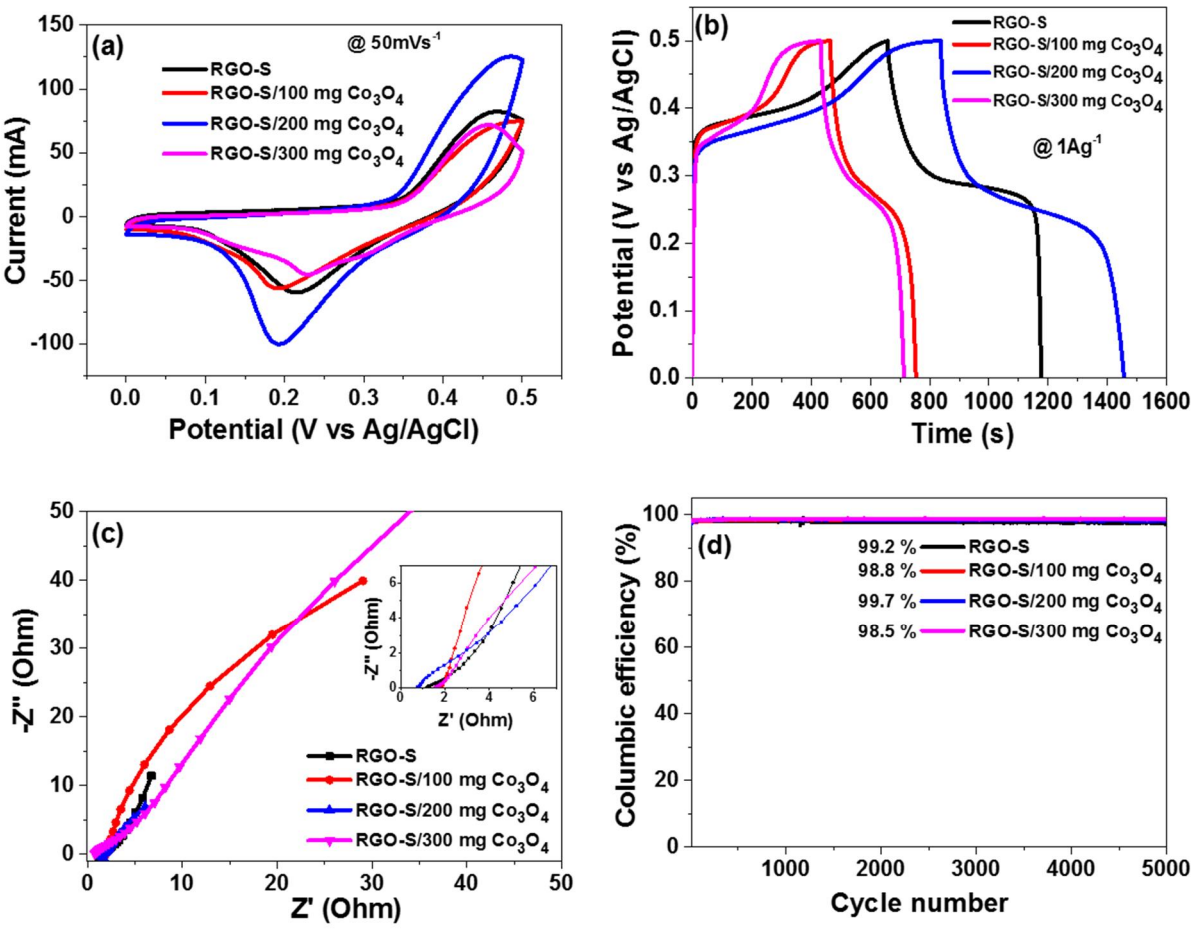

Fig. 6**:** (a) CV curves at 50 mV s^{-1} in a positive potential window, (b) GCD curves at 1 A g^{-1} in a positive potential window, (c) EIS Nyquist plot with an insert as the enlarged high-frequency region and (d) Cycling performance for RGO-S and RGO-S/Co_3O_4 composites in 1 M KOH, respectively.

For further investigation on the electrochemical measurements of RGO-S/200 mg Co_3O_4 composite sample, the CV analysis (Fig. 7 (a)) was done at various scan rates from 5 to 100 mV s^{-1} in a positive potential window range 0.0 - 0.5 V vs Ag/AgCl. The anodic peak around 0.26 V and cathodic peak around 0.42 V were displayed by the CV curve at low scan rate. This might be contributed by the hydroxyl, carboxyl, and epoxy functional group from RGO-S and redox properties from Co_3O_4 sample [55]. The increase in scan rate shows oxidation and reduction peaks were shifted in the direction of higher and lower potential, respectively indicating the development of charge diffusion polarization in a battery-type material [54]. The CV curves of RGO-S/200 mg Co_3O_4 using 1 M KOH electrolyte shows a pair of broad peaks

at about 0.26 V and 0.46 V, respectively. These peaks are due to the electron transfer between Co^{2+} and Co^{3+} ($Co^{2+}\leftrightarrow Co^{3+}$) and also S^{2+} and S^{4+} ($S^{2+}\leftrightarrow S^{4+}$) through the following redox reaction processes [18]:

$$Co_3O_4 + OH^- + H_2O \leftrightarrow 3CoOOH + e^- \quad (9)$$

$$CoOOH + OH^- \leftrightarrow CoO_2 + H_2O + e^- \quad (10)$$

$$S \leftrightarrow S^{2-} + 2e^- \quad (11)$$

The GCD curves (Fig. 7 (b)) of RGO-S/200 mg Co_3O_4 composite sample at various specific currents from 1 to 5 A g^{-1} corresponds well with the CV curves in Fig. 7 (a). The electrochemical redox reactions occur as a result of the interaction between the electrode and electrolyte in the material which produces redox peaks shown by the CV and GCD curves. In addition, a detailed analysis was conducted on EIS Nyquist plot. A representative EIS Nyquist plot comprises of two regions; a semicircle at high frequency and a straight line at low frequency region corresponding to charge transfer resistance (R_{CT}) and ion diffusion characteristics, respectively. Fig. 7 (c) displays the fitted EIS Nyquist plot of the composite material, with its corresponding circuit as the insert. The circuit is adopted for fitting the data and illustrates an equivalent series resistance (ESR), which is in series with charge transfer resistance (R_{CT}) at high-frequency region, and a Warburg (W) element that is in parallel with real capacitance (Q1). A mass capacitance (C3) is in parallel with the leakage resistance (R_L) at low frequency region. R_{CT} provides information about the reactions occurring between the interface of the electrode and electrolyte while R_L describes the Faradic charge transfer processes. The attained values of ESR =1.56 Ω and R_{CT} = 0.07 Ω for the electrode are comparable with the experimental values of ESR = 1.43 Ω and R_{CT} = 0.04 Ω, respectively, indicating perfect fitting of the Nyquist plot. The obtained small R_{CT} = 0.04 Ω shows low internal resistance and good electrical conductivity of the material. It is known that, the highest

specific power is inversely proportional to the ESR. Thus, reducing internal resistance is an important target in development of supercapattery with enhanced performances [1].

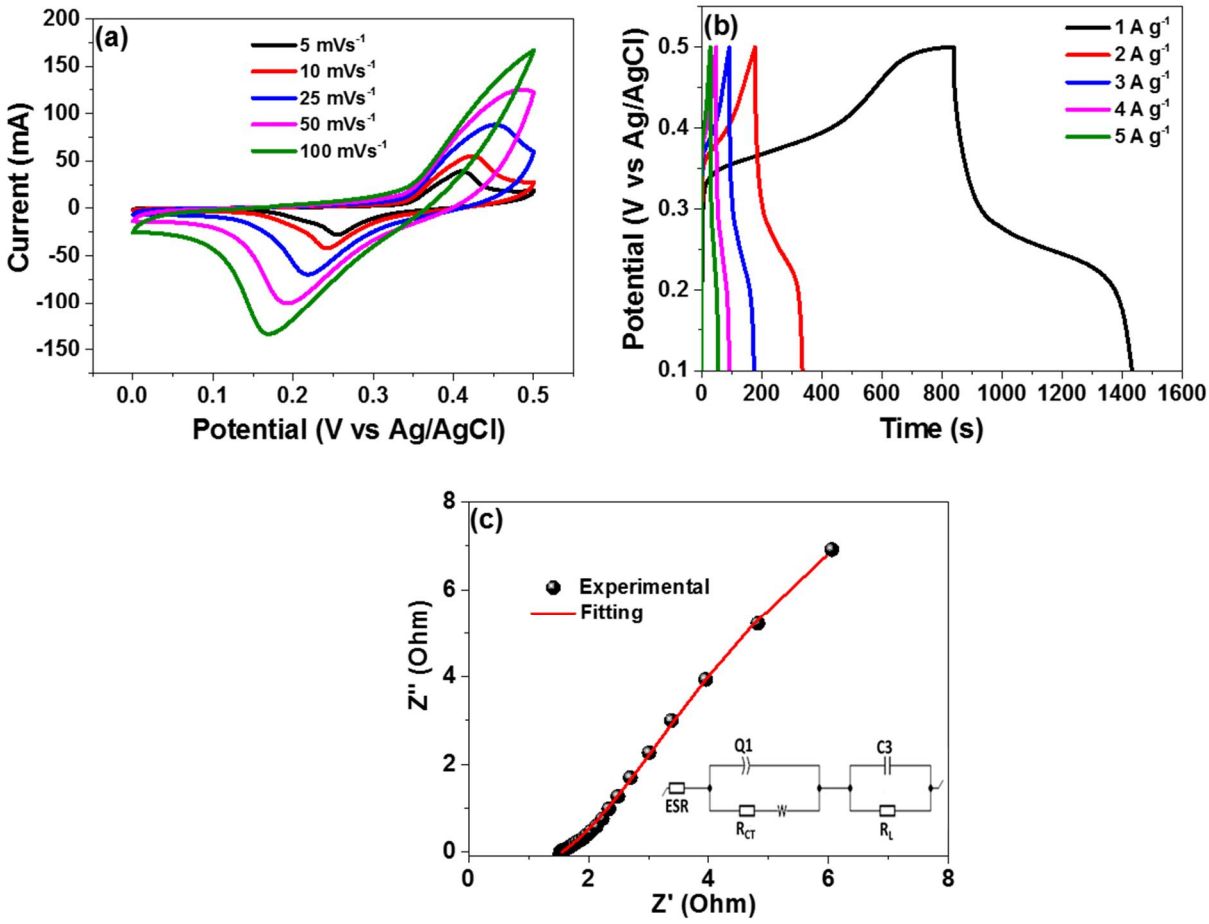

Fig. 7: (a) CV curves at different scan rates, (b) GCD curves at different specific current and (c) EIS Nyquist plot with an insert circuit for RGO-S/200 mg Co_3O_4 sample in 1 M KOH, respectively.

Since RGO-S/200 mg Co_3O_4 composite sample has shown superior electrochemical measurements compared to pristine and other composites samples, it was selected to investigate the practical applications of the material in supercapattery. The supercapattery device was designed using 1 M KOH electrolyte, RGO-S/200 mg Co_3O_4 composite as a positive electrode and activated carbon from peanut shell (AC-PS) as the negative electrode. AC-PS was selected as a negative electrode because it was found to have excellent electrochemical properties as detailed in our previous study [52]. Because of the variation in specific capacity/capacitance and the discharge time between the positive and negative

electrode, equation 5 was utilized to balance the mass of the electrodes by applying the charge balance as $Q_+ = Q_-$. The total mass of 5.4 mg/cm^2 corresponds to 2.0 mg and 3.4 mg, resulted from a mass balance ratio of 1.0:1.7 was estimated for RGO-S/200 mg Co_3O_4 and AC-PS, respectively. The assembled device was labelled as RGO-S/200 mg Co_3O_4//AC-PS.

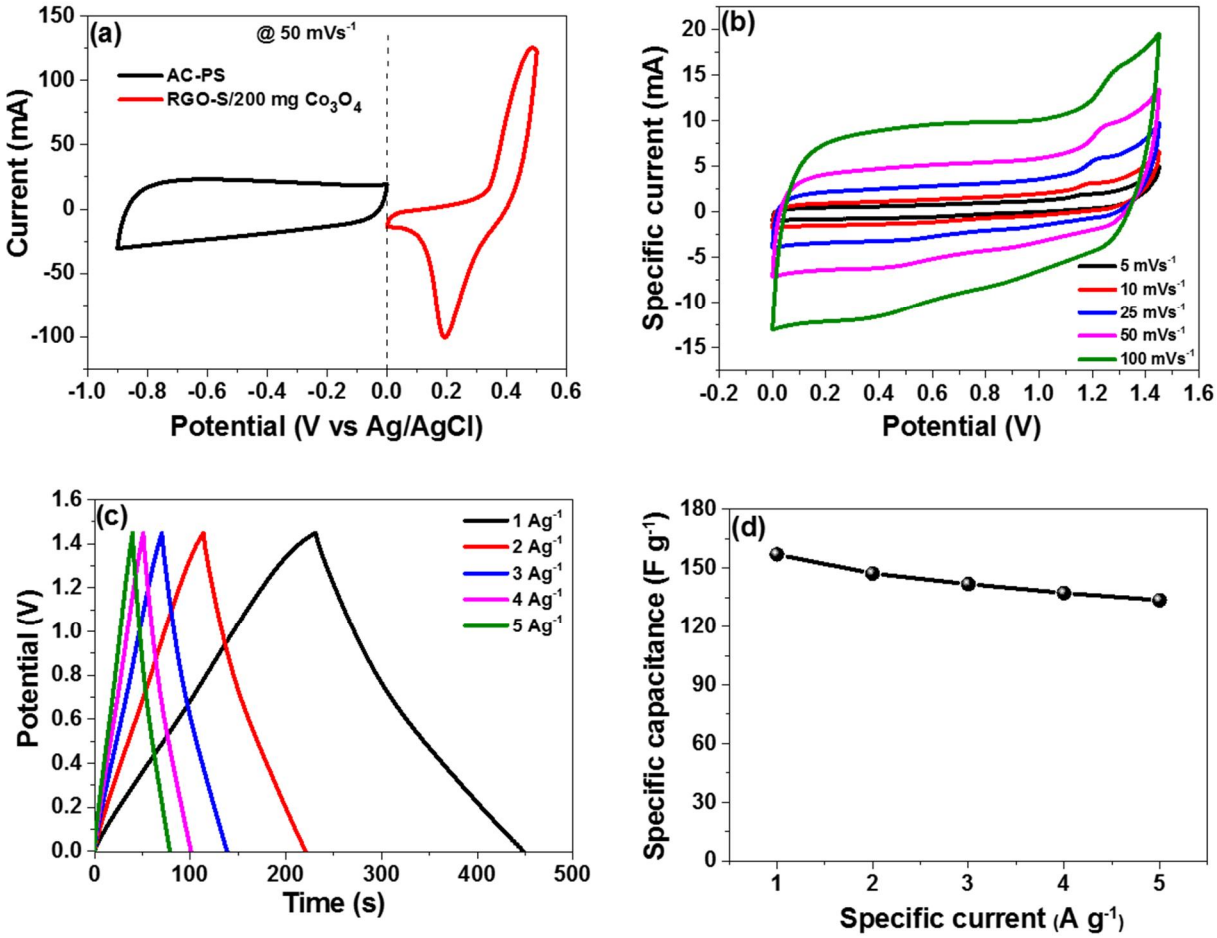

Fig. 8**:** (a) CV curves of RGO-S/200 mg Co_3O_4 and AC-PS electrodes in a positive and negative potential windows, respectively, (b) CV curves, (c) GCD curves and (d) Specific capacitance versus specific current for RGO-S/200 mg Co_3O_4//AC-PS in 1 M KOH, respectively.

Fig. 8 (a) show the CV curves at 50 mV s^{-1} for RGO-S/200 mg Co_3O_4 as a positive electrode in a positive potential window (0.0 - 0.5 V) displaying a faradic behaviour due to ongoing redox reaction, and AC-PS as a negative electrode showing EDLC shape indicating the capacitive behaviour of the material in a negative potential window (-0.9 - 0.0 V). The measurements performed at various scan rates from 5 to 100 mV s^{-1} in Fig. 8 (b) shows the CV curves of the device (RGO-S/200 mg Co_3O_4//AC-PS). The results confirm that the device is

more of pseudocapacitive behaviour whereby in terms of the current response still the Faradic positive electrode is pronounced, however, EDLC negative electrode has more influence because of the wide potential window. This kind of behaviour occurs when there is a good charge balancing signifying that electrode where charging and discharging at the same time regardless of their capacitive ability individually. A maximum cell potential window of 1.45 V, was produced by the assembled RGO-S/200 mg Co_3O_4//AC-PS device. The high rate capability of the material was confirmed by the current response in the CV curve which increases linearly as the scan rate increases without shape distortion [48]. Fig. 8 (c) presents the GCD curves of RGO-S/200 mg Co_3O_4//AC-PS at different specific currents. The GCD curves in Fig. 8 (b) are clearly pseudocapacitive with semi-linear curves confirming the two electrodes ended up with the so-called supercapattery device. It was further observed that the purely RGO-S/200 mg Co_3O_4 Faradic behaviour was transformed into pseudocapacitive behaviour by utilizing AC-PS as an EDLC material. This indicates that the synergetic effect of the EDLC (capacitive) and the Faradic (battery-type) material has resulted in a hybrid device with combined features, with the EDLC behaviour dominating because it had lower capacitance. Since the total capacitance of the device is the sum of the two capacitance in series as $C_T = 1/C_1 + 1/C_2$ then the material with lower capacitance will dominate and is termed as supercapattery. This is an emerging electrochemical energy storage devices, whereby a device is made up by combining the capacitive materials which store energy via adsorptions of ions and battery materials which store energy via faradic redox reactions to produce the final capacitive device [5,15,22,49]. The specific capacitance versus specific current for the RGO-S/200 mg Co_3O_4//AC-PS supercapattery device evaluated from the GCD profiles in Fig. 8 (c) using equation 6 is presented in Fig. 8 (d). It was observed that the supercapattery device was able to preserve the specific capacitance as the specific current increases because there was no

fast loss of the specific capacitance. Consequently, a rate capability of 85.1 % was preserved by the supercapattery device.

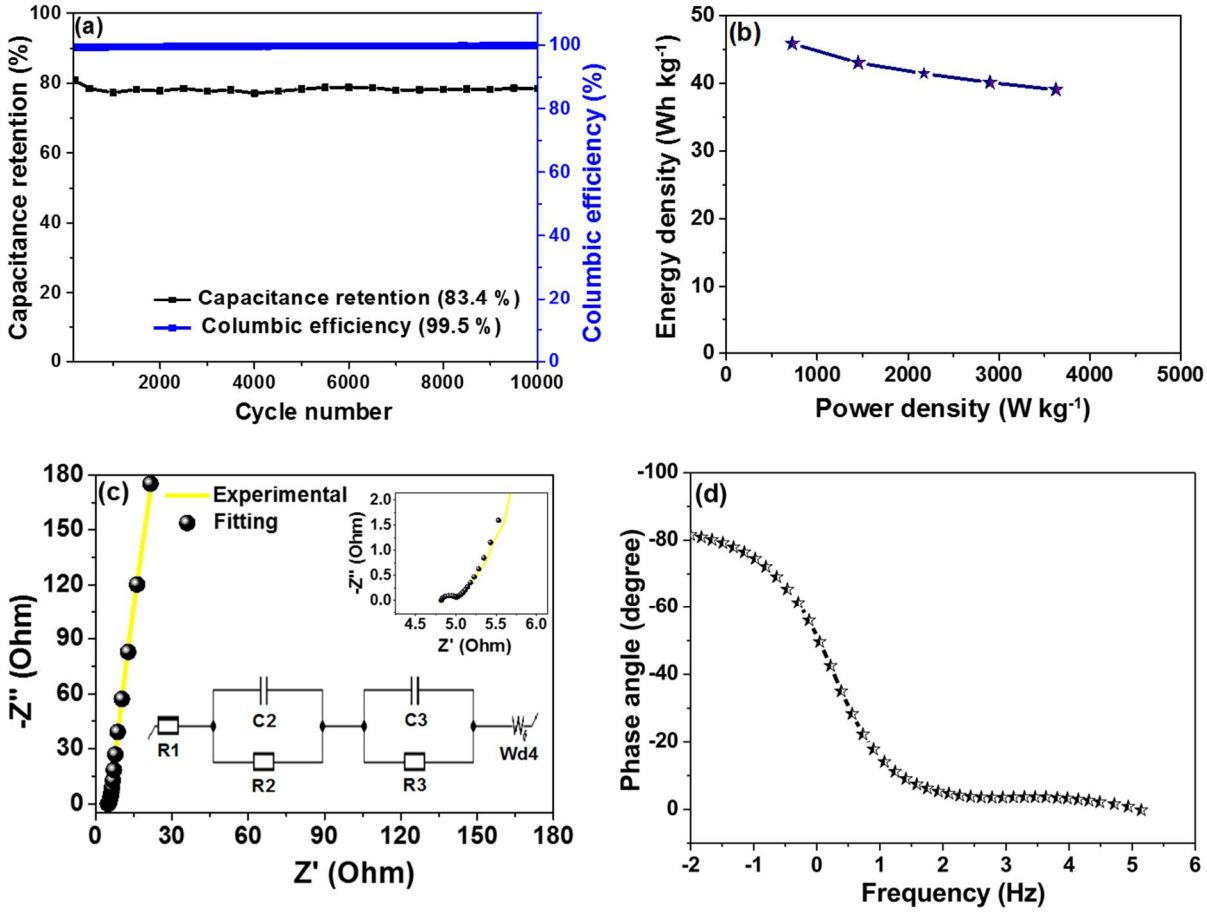

Fig. 9**:** (a) Capacitance retention and columbic efficiency versus cycle number (b) Ragone plot (c) EIS Nyquist plot (the insert shows an equivalent circuit applied for EIS fitting) and (d) Bode impedance of RGO-S/200 mg Co_3O_4//AC-PS sample, respectively in 1 M KOH.

Fig. 9 (a) display long cycling performance of up to 10, 000 cycles applied to evaluate the stability of the RGO-S/200 mg Co_3O_4//AC-PS supercapattery device. The RGO-S/200 mg Co_3O_4//AC-PS supercapattery device revealed a capacitance retention and columbic efficiency of 83.4 % and 99.5 %, respectively at 8 A g^{-1} over 10, 000 cycles. This good cycling performance could be due to the good synergy between Co_3O_4 and RGO-S, which resulted in a repeated contraction and expansion of the electrodes during charging-discharging cycles. Therefore, this shows that there was an improvement in wettability which allows accessibility of ions within the material [61]. Equations 7 and 8 were employed to evaluate the specific

energy and power for RGO-S/200 mg Co_3O_4//AC-PS supercapattery device and results are presented in Fig. 9 (b) as a Ragone plot. The highest specific energy recorded at 1 A g^{-1} was 45.8 Wh kg^{-1} with its corresponding specific power of 725 W kg^{-1}. The fabricated RGO-S/200 mg Co_3O_4//AC-PS supercapattery device revealed higher value of specific energy and power compared to some similar materials reported recently in the literature as shown in Table 1 below.

Fig. 9 (c) display Nyquist plot showing fitting and experimental data plotted together for RGO-S/200 mg Co_3O_4//AC-PS supercapattery device. The EIS fitting circuit obtained by the Z fit software from the EC-lab 10.40 is displayed by the insert to Fig. 9 (c) presenting a linear line close to be parallel to y-axis at low-frequency region and a small semicircle at high-frequency region. From the circuit, R1, R2 and R3 present equivalent series resistance (ESR), charge transfer resistance and leakage resistance, respectively. Whereas, C2 and C3 indicate real and mass capacitance, respectively. R2 and C2 provides information about the resistance rate and Faradic electrochemical activity which takes place between the electrode and electrolyte while R3 and C3 gives information about the resistance and capacitance associated with EDLC. The ESR (represented as R1 in the circuit) was estimated experimentally at high-frequency region while the lower charge transfer resistance is confirmed by a very small semicircle at higher frequency region as presented by the inset to Fig. 9 (c). The experimental values for the equivalent series resistance (R1) and charge transfer resistance (R2) were 4.78 and 0.16 Ω, respectively, which were comparable to the values obtained through fitting as 4.82 and 0.19 Ω, respectively. Other parameters recorded from the fitting circuit were R3, C2, C3 and Wd4 with 0.16 Ω, 0.092 F, 0.054 F and 5.9 Ω values, respectively. Furthermore, the response recorded from the Nyquist plot shows the curve is almost parallel to the imaginary impedance (-Z") axis, which is evidence that the device is very close to the ideal capacitance behaviour. Fig. 8 (d)

illustrates the phase angle versus frequency profile with an ideal value of -90^0 in which the RGO-S/200 mg Co_3O_4//AC-PS supercapattery device is at -81.6^0.

Table 1: Comparisons of electrochemical performance (cycle life, energy and power density) of some similar materials from the literature calculated from two electrode systems

Electrodes (Device)	**Electrolyte**	**Energy density**	**Power density**	**Cycle life**	**Ref.**
Co_3O_4/C//Co_3O_4/C	2 M KOH	23.4 Wh kg^{-1}	162.5 W kg^{-1}	-	[50]
Co_3O_4-rGO//AC	6 M KOH	35.7 Wh kg^{-1}	225 W kg^{-1}	1000	[20]
MWCNT-Co_3O_4-Ag//AC	1 M KOH	16.5 Wh kg^{-1}	297.5 W kg^{-1}	3000	[22]
Co_3O_4//Co_3O_4	2 M KOH	25.5 Wh kg^{-1}	11 kW kg^{-1}	4000	[46]
Co_3O_4-T//AC	6 M KOH	42.81 Wh kg^{-1}	1.69 kW kg^{-1}	1000	[28]
MOF/PANI/AC	1 M KOH	23.2 Wh kg^{-1}	1600 Wh kg^{-1}	3000	[62]
Co_3O_4//rGO	1 M KOH	40 Wh kg^{-1}	742 W kg^{-1}	5000	[27]
$MnCo_2O_4$//AC	6 M KOH	33.8 Wh kg^{-1}	318.9 W kg^{-1}	10,000	[25]
rGO-Co_3O_4-Ag//AC	1 M KOH	23.63 Wh kg^{-1}	440 W kg^{-1}	3000	[26]
Co_3O_4 nano flakes//AC	1 M KOH	23.7 Wh kg^{-1}	307 W kg^{-1}	2500	[24]
RGO-S/200 mg Co_3O_4//AC-PS	**1 M KOH**	**45.8 Wh kg^{-1}**	**725 W kg^{-1}**	**10,000**	**This work**

Fig. 10 (a) shows a specific capacitance versus floating time for the supercapattery device exposed to the highest voltage of 1.45 V for over 150 h at 10 A g^{-1}. After every 10 h the specific capacitance was monitored and the device was able to withstand a stability of 71.6 % after 150 h. This superior cycling achievement could be associated with the chemically stable structure of the combined features of RGO-S and Co_3O_4. Also, Co_3O_4 act as a spacer to stabilize RGO-S whose interlayer spacing are extended when Co_3O_4 is incorporated [55]. The CV and GCD curves of RGO-S/200 mg Co_3O_4//AC-PS supercapattery device before and after voltage holding, respectively, are displayed in Fig. 10 (b and c). It was observed that after 150 h of

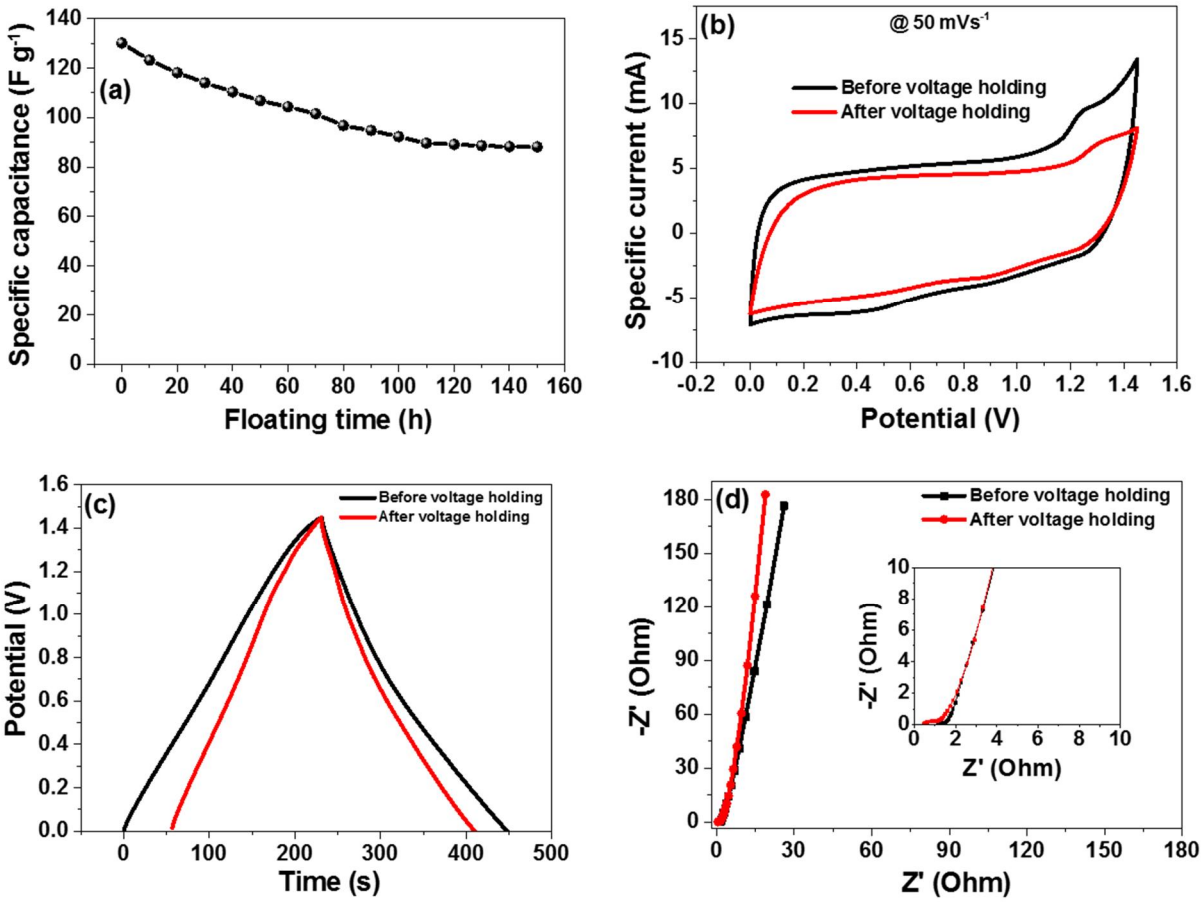

Fig. 10: (a) Floating time versus specific capacitance, (b) CV curves before and after voltage holding at 50 mV s^{-1}, (c) CD curves before and after voltage holding at 1 A g^{-1} and (d) EIS Nyquist plot before and after voltage holding for RGO-S/200 mg Co_3O_4//AC-PS sample in 1 M KOH, respectively.

cycling the shape was maintained, however, the current response in the CV curve and discharge time in the GCD curve slightly decreased after the device being subjected to many cycles. This proves good stability of the device which is attributed to the synergetic effect of the two materials. The RGO-S/200 mg Co_3O_4//AC-PS supercapattery device displayed an EIS Nyquist plot before and after voltage holding as observed in Fig. 10 (d). The figure revealed that after voltage holding there was an improvement in the equivalent series resistance from 1.04 Ω to 0.52 Ω. Also, the vertical line is considerably closer to the y-axis indicating an improvement in the capacitive behaviour of the device. This shows that more ions managed to access more pores of the material. Furthermore, the interaction of Co_3O_4 and RGO-S allows the insertion

and de-insertion of the electrolyte ions within the material, thus inhibit its aggregation and minimize the charge transfer resistance of the device [55].

4. CONCLUSION

Sulphur-reduced graphene oxide/cobalt oxide composites (RGO-S/Co_3O_4) were successfully synthesized via a simple hydrothermal method. The micrographs, structural, chemical composition, and functional group analysis indicated the successful synthesis of RGO-S and RGO-S/Co_3O_4 composite samples. An optimized RGO-S/200 mg Co_3O_4 composite presented the highest specific capacity of 171.8 mAh g^{-1} and superior stability of 99.7 % over 5000 cycles at 1 and 5 A g^{-1}, respectively, using 1 M KOH electrolyte in a three-electrode system. The fabricated supercapattery device, RGO-S/200 mg Co_3O_4//AC-PS demonstrated a high specific energy and power of 45.8 Wh kg^{-1} and 725 W kg^{-1}, respectively, at 1 A g^{-1}. The device was able to retain about 83.4 % of its initial capacitance and 99.5 % of the columbic efficiency for over 10, 000 cycles. An outstanding cycling performance of 71.6 % was sustained from the voltage holding test performed for over 150 h at 10 A g^{-1}. The results demonstrated excellent synergy between optimized Co_3O_4 and RGO-S which led to the supercapattery device when combined with activated carbon from the peanut shell.

ACKNOWLEDGEMENTS

This work is based on the research supported by the South African Research Chairs Initiative of the Department of Science and Technology (DST) and National Research Foundation (NRF) of South Africa (Grant No. 61056). Any opinion, finding, and conclusion expressed in this material are that of the authors, and the DST and NRF do not accept any liability in this regard. Delvina Japhet Tarimo acknowledges the financial support from NRF through SARChI chair in Carbon Technology and Materials. Delvina Japhet Tarimo thanks the African-German

Network of Excellence in Science (AGNES) for granting a Mobility Grant in 2019; the Grant is generously sponsored by German Federal Ministry of Education and Research and supported by the Alexander von Humboldt Foundation. Dr Cosmas Muiva of the Department of Physics, Botswana International University of Science and Technology, Botswana is acknowledged as a host supervisor during the visit.

REFERENCES

[1] Yin JL, Park JY. Electrochemical investigation of copper/nickel oxide composites for supercapacitor applications. Int J Hydrogen Energy 2014;39:16562–8. doi:10.1016/j.ijhydene.2014.04.202.

[2] Krishnamoorthy K, Thangavel S, Chelora Veetil J, Raju N, Venugopal G, Kim SJ. Graphdiyne nanostructures as a new electrode material for electrochemical supercapacitors. Int J Hydrogen Energy 2016;41:1672–8. doi:10.1016/j.ijhydene.2015.10.118.

[3] Numan A, Duraisamy N, Saiha Omar F, Mahipal YK, Ramesh K, Ramesh S. Enhanced electrochemical performance of cobalt oxide nanocube intercalated reduced graphene oxide for supercapacitor application. RSC Adv 2016;6:34894–902. doi:10.1039/c6ra00160b.

[4] Huo J, Zheng P, Wang X, Guo S. Three-dimensional sulphur/nitrogen co-doped reduced graphene oxide as high-performance supercapacitor binder-free electrodes. Appl Surf Sci 2018;442:575–80. doi:10.1016/j.apsusc.2018.01.221.

[5] Chen GZ. Supercapacitor and supercapattery as emerging electrochemical energy stores. Int Mater Rev 2017;62:173–202. doi:10.1080/09506608.2016.1240914.

[6] Wang JP, Wang SL, Huang ZC, Yu YM, Liu JL. Synthesis of long chain-like nickel cobalt oxide nanoneedles-reduced graphene oxide composite material for high-

performance supercapacitors. Ceram Int 2014;40:12751–8. doi:10.1016/j.ceramint.2014.04.128.

[7] Lamiel C, Lee YR, Cho MH, Tuma D, Shim JJ. Enhanced electrochemical performance of nickel-cobalt-oxide@reduced graphene oxide//activated carbon asymmetric supercapacitors by the addition of a redox-active electrolyte. J Colloid Interface Sci 2017;507:300–9. doi:10.1016/j.jcis.2017.08.003.

[8] Ke Q, Tang C, Yang ZC, Zheng M, Mao L, Liu H, et al. 3D nanostructure of carbon nanotubes decorated Co_3O_4 nanowire arrays for high performance supercapacitor electrode. Electrochim Acta 2015;163:9–15. doi:10.1016/j.electacta.2015.02.136.

[9] Chen YY, Dhaiveegan P, Michalska M, Lin JY. Morphology-controlled synthesis of nanosphere-like $NiCo_2S_4$ as cathode materials for high-rate asymmetric supercapacitors. Electrochim Acta 2018;274:208–16. doi:10.1016/j.electacta.2018.04.086.

[10] García-Gómez A, Eugénio S, Duarte RG, Silva TM, Carmezim MJ, Montemor MF. Electrodeposited reduced-graphene oxide/cobalt oxide electrodes for charge storage applications. Appl Surf Sci 2016;382:34–40. doi:10.1016/j.apsusc.2016.04.113.

[11] García-Gómez A, Duarte RG, Eugénio S, Silva TM, Carmezim MJ, Montemor MF. Fabrication of electrochemically reduced graphene oxide/cobalt oxide composite for charge storage electrodes. J Electroanal Chem 2015;755:151–7. doi:10.1016/j.jelechem.2015.07.053.

[12] Ramesh S, Karuppasamy K, Kim HS, Kim HS, Kim JH. Hierarchical Flowerlike 3D nanostructure of Co3O4@MnO2/N-doped Graphene oxide (NGO) hybrid composite for a high-performance supercapacitor. Sci Rep 2018;8:1–11. doi:10.1038/s41598-018-34905-7.

[13] García-Gómez A, Eugénio S, Duarte RG, Silva TM, Carmezim MJ, Montemor MF.

Electrodeposited reduced-graphene oxide/cobalt oxide electrodes for charge storage applications. Appl Surf Sci 2016;382:34–40. doi:10.1016/j.apsusc.2016.04.113.

[14] Wang HW, Hu ZA, Chang YQ, Chen YL, Zhang ZY, Yang YY, et al. Preparation of reduced graphene oxide/cobalt oxide composites and their enhanced capacitive behaviors by homogeneous incorporation of reduced graphene oxide sheets in cobalt oxide matrix. Mater Chem Phys 2011;130:672–9. doi:10.1016/j.matchemphys.2011.07.043.

[15] Omar FS, Numan A, Bashir S, Duraisamy N, Vikneswaran R, Loo YL, et al. Enhancing rate capability of amorphous nickel phosphate supercapattery electrode via composition with crystalline silver phosphate. Electrochim Acta 2018;273:216–28. doi:10.1016/j.electacta.2018.03.136.

[16] Jokar E, Iraji zad A, Shahrokhian S. Growth control of cobalt oxide nanoparticles on reduced graphene oxide for enhancement of electrochemical capacitance. Int J Hydrogen Energy 2014;39:21068–75. doi:10.1016/j.ijhydene.2014.10.061.

[17] García-Gómez A, Duarte RG, Eugénio S, Silva TM, Carmezim MJ, Montemor MF. Fabrication of electrochemically reduced graphene oxide/cobalt oxide composite for charge storage electrodes. J Electroanal Chem 2015;755:151–7. doi:10.1016/j.jelechem.2015.07.053.

[18] Xiang C, Li M, Zhi M, Manivannan A, Wu N. A reduced graphene oxide/Co3O4 composite for supercapacitor electrode. J Power Sources 2013;226:65–70. doi:10.1016/j.jpowsour.2012.10.064.

[19] Song Z, Zhang Y, Liu W, Zhang S, Liu G, Chen H, et al. Hydrothermal synthesis and electrochemical performance of Co 3O4/reduced graphene oxide nanosheet composites for supercapacitors. Electrochim Acta 2013;112:120–6. doi:10.1016/j.electacta.2013.08.155.

[20] Xie LJ, Wu JF, Chen CM, Zhang CM, Wan L, Wang JL, et al. A novel asymmetric supercapacitor with an activated carbon cathode and a reduced graphene oxide-cobalt oxide nanocomposite anode. J Power Sources 2013;242:148–56. doi:10.1016/j.jpowsour.2013.05.081.

[21] Huo J, Zheng P, Wang X, Guo S. Three-dimensional sulphur/nitrogen co-doped reduced graphene oxide as high-performance supercapacitor binder-free electrodes. Appl Surf Sci 2018;442:575–80. doi:10.1016/j.apsusc.2018.01.221.

[22] Iqbal J, Numan A, Rafique S, Jafer R, Mohamad S, Ramesh K, et al. High performance supercapattery incorporating ternary nanocomposite of multiwalled carbon nanotubes decorated with Co3O4 nanograins and silver nanoparticles as electrode material. Electrochim Acta 2018;278:72–82. doi:10.1016/j.electacta.2018.05.040.

[23] Noori A, El-Kady MF, Rahmanifar MS, Kaner RB, Mousavi MF. Towards establishing standard performance metrics for batteries, supercapacitors and beyond. Chem Soc Rev 2019;48:1272–341. doi:10.1039/c8cs00581h.

[24] Numan A, Ramesh kumar P, Khalid M, Ramesh S, Ramesh K, Shamsudin EM, et al. Facile sonochemical synthesis of 2D porous Co3O4 nanoflake for supercapattery. J Alloys Compd 2020;819:153019. doi:10.1016/j.jallcom.2019.153019.

[25] Saravanakumar B, Wang X, Zhang W, Xing L, Li W. Holey two dimensional manganese cobalt oxide nanosheets as a high-performance electrode for supercapattery. Chem Eng J 2019;373:547–55. doi:10.1016/j.cej.2019.05.080.

[26] Iqbal J, Numan A, Jafer R, Bashir S, Jilani A, Mohammad S, et al. Ternary nanocomposite of cobalt oxide nanograins and silver nanoparticles grown on reduced graphene oxide conducting platform for high-performance supercapattery electrode material. J Alloys Compd 2020;821:153452. doi:10.1016/j.jallcom.2019.153452.

[27] Sankar Devi V, Athika M, Duraisamy E, Prasath A, Selva Sharma A, Elumalai P. Facile sol-gel derived nanostructured spinel Co3O4 as electrode material for high-performance supercapattery and lithium-ion storage. J Energy Storage 2019;25:100815. doi:10.1016/j.est.2019.100815.

[28] Meng T, Xu QQ, Wang ZH, Li YT, Gao ZM, Xing XY, et al. Co3O4 Nanorods with Self-assembled Nanoparticles in Queue for Supercapacitor. Electrochim Acta 2015;180:104–11. doi:10.1016/j.electacta.2015.08.085.

[29] Lamiel C, Lee YR, Cho MH, Tuma D, Shim JJ. Enhanced electrochemical performance of nickel-cobalt-oxide@reduced graphene oxide//activated carbon asymmetric supercapacitors by the addition of a redox-active electrolyte. J Colloid Interface Sci 2017;507:300–9. doi:10.1016/j.jcis.2017.08.003.

[30] Liu H, Gou X, Wang Y, Du X, Quan C, Qi T. Cauliflower-Like Co3O4/Three-Dimensional Graphene Composite for High Performance Supercapacitor Applications. J Nanomater 2015;2015. doi:10.1155/2015/874245.

[31] Halder A, Zhang M, Chi Q. Electrocatalytic Applications of Graphene–Metal Oxide Nanohybrid Materials. Adv Catal Mater - Photocatal Other Curr Trends 2016. doi:10.5772/61808.

[32] Kiciński W, Szala M, Bystrzejewski M. Sulfur-doped porous carbons: Synthesis and applications. Carbon N Y 2014;68:1–32. doi:10.1016/j.carbon.2013.11.004.

[33] Bai Y, Lu L, Bao J, Sun G, Zhang B, Zeng J, et al. The preparation and electrochemical performance of nitrogen-doped graphene/Co(OH)2 composite. Int J Electrochem Sci 2019;14:606–17. doi:10.20964/2019.01.48.

[34] Xie LJ, Wu JF, Chen CM, Zhang CM, Wan L, Wang JL, et al. A novel asymmetric supercapacitor with an activated carbon cathode and a reduced graphene oxide-cobalt oxide nanocomposite anode. J Power Sources 2013;242:148–56.

doi:10.1016/j.jpowsour.2013.05.081.

[35] Jokar E, Iraji zad A, Shahrokhian S. Growth control of cobalt oxide nanoparticles on reduced graphene oxide for enhancement of electrochemical capacitance. Int J Hydrogen Energy 2014;39:21068–75. doi:10.1016/j.ijhydene.2014.10.061.

[36] Yoo MJ, Park HB. Effect of hydrogen peroxide on properties of graphene oxide in Hummers method. Carbon N Y 2019;141:515–22. doi:10.1016/j.carbon.2018.10.009.

[37] Li Z, Li C, Ge X, Ma J, Zhang Z, Li Q, et al. Reduced graphene oxide wrapped MOFs-derived cobalt-doped porous carbon polyhedrons as sulfur immobilizers as cathodes for high performance lithium sulfur batteries. Nano Energy 2016;23:15–26. doi:10.1016/j.nanoen.2016.02.049.

[38] Yu X, Park SK, Yeon SH, Park HS. Three-dimensional, sulfur-incorporated graphene aerogels for the enhanced performances of pseudocapacitive electrodes. J Power Sources 2015;278:484–9. doi:10.1016/j.jpowsour.2014.12.102.

[39] Tian Z, Li J, Zhu G, Lu J, Wang Y, Shi Z, et al. Facile synthesis of highly conductive sulfur-doped reduced graphene oxide sheets. Phys Chem Chem Phys 2015;18:1125–30. doi:10.1039/c5cp05475c.

[40] Tarimo DJ, Oyedotun KO, Mirghni AA, Sylla NF, Manyala N. High energy and excellent stability asymmetric supercapacitor derived from sulphur-reduced graphene oxide/manganese dioxide composite and activated carbon from peanut shell. Electrochim Acta 2020;353:136498. doi:10.1016/j.electacta.2020.136498.

[41] Wang JP, Wang SL, Huang ZC, Yu YM, Liu JL. Synthesis of long chain-like nickel cobalt oxide nanoneedles-reduced graphene oxide composite material for high-performance supercapacitors. Ceram Int 2014;40:12751–8. doi:10.1016/j.ceramint.2014.04.128.

[42] Edison TNJI, Atchudan R, Sethuraman MG, Lee YR. Supercapacitor performance of

carbon supported Co3O4 nanoparticles synthesized using Terminalia chebula fruit. J Taiwan Inst Chem Eng 2016;68:489–95. doi:10.1016/j.jtice.2016.09.021.

[43] Numan A, Shahid MM, Omar FS, Ramesh K, Ramesh S. Facile fabrication of cobalt oxide nanograin-decorated reduced graphene oxide composite as ultrasensitive platform for dopamine detection. Sensors Actuators, B Chem 2017;238:1043–51. doi:10.1016/j.snb.2016.07.111.

[44] Song Z, Zhang Y, Liu W, Zhang S, Liu G, Chen H, et al. Hydrothermal synthesis and electrochemical performance of Co 3O4/reduced graphene oxide nanosheet composites for supercapacitors. Electrochim Acta 2013;112:120–6. doi:10.1016/j.electacta.2013.08.155.

[45] Nguyen TT, Nguyen VH, Deivasigamani RK, Kharismadewi D, Iwai Y, Shim JJ. Facile synthesis of cobalt oxide/reduced graphene oxide composites for electrochemical capacitor and sensor applications. Solid State Sci 2016;53:71–7. doi:10.1016/j.solidstatesciences.2016.01.006.

[46] Xia XH, Tu JP, Zhang YQ, Mai YJ, Wang XL, Gu CD, et al. Freestanding Co 3O 4 nanowire array for high performance supercapacitors. RSC Adv 2012;2:1835–41. doi:10.1039/c1ra00771h.

[47] Li Z, Li C, Ge X, Ma J, Zhang Z, Li Q, et al. Reduced graphene oxide wrapped MOFs-derived cobalt-doped porous carbon polyhedrons as sulfur immobilizers as cathodes for high performance lithium sulfur batteries. Nano Energy 2016;23:15–26. doi:10.1016/j.nanoen.2016.02.049.

[48] Naveen AN, Manimaran P, Selladurai S. Cobalt oxide (Co3O4)/graphene nanosheets (GNS) composite prepared by novel route for supercapacitor application. J Mater Sci Mater Electron 2015;26:8988–9000. doi:10.1007/s10854-015-3582-2.

[49] William JJ, Babu IM, Muralidharan G. Spongy structured α-Ni(OH)2: Facile and rapid

synthesis for supercapattery applications. Mater Lett 2019;238:35–7. doi:10.1016/j.matlet.2018.11.136.

[50] Balasubramanian S, Kamatchi Kamaraj P. Fabrication of natural polymer assisted mesoporous Co3O4/carbon composites for supercapacitors. Electrochim Acta 2015;168:50–8. doi:10.1016/j.electacta.2015.04.019.

[51] Tarimo DJ, Oyedotun KO, Mirghni AA, Manyala N. Sulphur-reduced graphene oxide composite with improved electrochemical performance for supercapacitor applications. Int J Hydrogen Energy 2020;45:13189–201. doi:10.1016/j.ijhydene.2020.03.059.

[52] Sylla NF, Ndiaye NM, Ngom BD, Momodu D, Madito MJ, Mutuma BK, et al. Effect of porosity enhancing agents on the electrochemical performance of high-energy ultracapacitor electrodes derived from peanut shell waste. Sci Rep 2019;9:1–15. doi:10.1038/s41598-019-50189-x.

[53] Mirghni AA, Oyedotun KO, Mahmoud BA, Bello A, Ray SC, Manyala N. Nickel-cobalt phosphate/graphene foam as enhanced electrode for hybrid supercapacitor. Compos Part B Eng 2019;174:106953. doi:10.1016/j.compositesb.2019.106953.

[54] Oyedotun KO, Madito MJ, Momodu DY, Mirghni AA, Masikhwa TM, Manyala N. Synthesis of ternary NiCo-MnO2 nanocomposite and its application as a novel high energy supercapattery device. Chem Eng J 2018;335:416–33. doi:10.1016/j.cej.2017.10.169.

[55] Wang B, Wang Y, Park J, Ahn H, Wang G. In situ synthesis of Co3O4/graphene nanocomposite material for lithium-ion batteries and supercapacitors with high capacity and supercapacitance. J Alloys Compd 2011;509:7778–83. doi:10.1016/j.jallcom.2011.04.152.

[56] Tang CW, Wang C Bin, Chien SH. Characterization of cobalt oxides studied by FT-

IR, Raman, TPR and TG-MS. Thermochim Acta 2008;473:68–73. doi:10.1016/j.tca.2008.04.015.

[57] Guo Y, Zhao J, Yang S, Yu K, Wang Z, Zhang H. Preparation and characterization of monoclinic sulfur nanoparticles by water-in-oil microemulsions technique. Powder Technol 2006;162:83–6. doi:10.1016/j.powtec.2005.12.012.

[58] Nguyen TT, Nguyen VH, Deivasigamani RK, Kharismadewi D, Iwai Y, Shim JJ. Facile synthesis of cobalt oxide/reduced graphene oxide composites for electrochemical capacitor and sensor applications. Solid State Sci 2016;53:71–7. doi:10.1016/j.solidstatesciences.2016.01.006.

[59] Tan Y, Gao Q, Yang C, Yang K, Tian W, Zhu L. One-dimensional porous nanofibers of Co3O4 on the carbon matrix from human hair with superior lithium ion storage performance. Sci Rep 2015;5:15–7. doi:10.1038/srep12382.

[60] Tarimo DJ, Oyedotun KO, Mirghni AA, Manyala N. Sulphur-reduced graphene oxide composite with improved electrochemical performance for supercapacitor applications. Int J Hydrogen Energy 2020;45. doi:10.1016/j.ijhydene.2020.03.059.

[61] Li Q, Hu X, Yang Q, Yan Z, Kang L, Lei Z, et al. Electrocapacitive performance of graphene/Co3O4 hybrid material prepared by a nanosheet assembly route. Electrochim Acta 2014;119:184–91. doi:10.1016/j.electacta.2013.12.066.

[62] Iqbal MZ, Faisal MM, Ali SR, Farid S, Afzal AM. Co-MOF/polyaniline-based electrode material for high performance supercapattery devices. Electrochim Acta 2020;346:136039. doi:10.1016/j.electacta.2020.136039.